Title: A Brain Reward Circuit Inhibited By Next-Generation Weight Loss Drugs

Authors

Elizabeth N. Godschall[1†], Taha Bugra Gungul[1†], Isabelle R. Sajonia[1†], Aleyna K. Buyukaksakal[1], Sophia Ogilvie[1], Austin B. Keeler[1], YuChen Zhang[2], Tyler C. J. Deutsch[3], Yu Shi[1], Nicholas J. Conley[2], Addison N. Webster[2], O. Yipkin Calhan[1], Amani Akkoub[1], Karan Malik[1], Kaleigh I. West[1], Arun Karthikeyan[1], Grace van Gerven[1], Manoj K. Patel[3], John N. Campbell[1,2,4], Christopher D. Deppmann[1,2,4-6]*, Ali D. Güler[1,2,4]*

[1]Department of Biology, University of Virginia; Charlottesville, VA 22904, USA.
[2]Department of Neuroscience, School of Medicine, University of Virginia; Charlottesville, VA 22903, USA.
[3]Department of Anesthesiology, University of Virginia Health System, Charlottesville, VA 22904, USA.
[4]Program in Fundamental Neuroscience; Charlottesville, VA 22904, USA.
[5]Department of Cell Biology, University of Virginia; Charlottesville, VA 22904, USA.
[6]Department of Biomedical Engineering, University of Virginia; Charlottesville, VA 22904, USA.

*Corresponding author. Email: aguler@virginia.edu and deppmann@virginia.edu.

[†]These authors contributed equally to this work.

Abstract

Glucagon-like peptide-1 receptor agonists (GLP1RAs) effectively reduce body weight and improve metabolic outcomes, yet established peptide-based therapies require injections and complex manufacturing. Small-molecule GLP1RAs promise oral bioavailability and scalable manufacturing, but their selective binding to human versus rodent receptors has limited mechanistic studies. The neural circuits through which these emerging therapeutics modulate feeding behavior remain undefined, particularly in comparison to established peptide-based GLP1RAs. Here, we developed humanized GLP1R mouse models to investigate how small-molecule GLP1RAs influence feeding behavior. Integrating genetic manipulations, calcium imaging, and behavior profiling, we discovered that these compounds regulate both homeostatic and hedonic feeding through parallel neural circuits. Beyond engaging canonical hypothalamic and hindbrain networks that control metabolic homeostasis, GLP1RAs recruit a discrete population of Glp1r-expressing neurons in the central amygdala, which selectively suppress the consumption of palatable foods by reducing dopamine release in the nucleus accumbens. Stimulating these central amygdalar neurons curtail hedonic feeding, whereas targeted deletion of the receptor in this cell population specifically diminishes the anorectic efficacy of GLP1RAs for reward-driven intake. These findings reveal a dedicated neural circuit through which small molecule GLP1RAs modulate reward processing, suggesting broad therapeutic potential in conditions of dysregulated dopamine signaling including substance use disorder and binge eating.

Main

The global obesity epidemic has catalyzed an urgent search for effective pharmacological interventions, with glucagon-like peptide-1 receptor agonists (GLP1RAs) emerging as leading candidates. These compounds, notably liraglutide (Saxenda, Victoza) and semaglutide (Wegovy, Ozempic), promote weight loss by enhancing insulin secretion, suppressing glucagon release, and inducing satiety (**Fig. 1a,b**) [1–5,1,6,7–17]. Recent studies have highlighted crucial roles for hypothalamic and hindbrain regions in GLP1RA-mediated feeding suppression[18–25]. However, peptide-based GLP1RAs require injection, cold storage, and complex manufacturing processes, with widespread global supply chain issues restricting patient access[26–29]. Next-generation small-molecule GLP1RAs like danuglipron (PF06882961) and orforglipron (LY3502970) offer transformative advantages through oral bioavailability and scalable manufacturing (**Fig. 1a**)[30,31–36]. Yet a critical challenge in developing these compounds has been their species-specific binding properties—many small-molecule GLP1RAs that effectively activate human GLP1R show minimal activity at rodent receptors, severely limiting preclinical investigation of their mechanisms of action[35,37,38,39]. Notably, orforglipron has advanced into over ten registered Phase 3 clinical trials[31–33,40]. The imminent clinical deployment of these small-molecules demands urgent investigation of their neural mechanisms, particularly given emerging evidence of GLP1RAs' effects on mood, motivation, and reward processing[41–45]. To overcome the species specificity of small-molecule GLP1RAs and enable preclinical investigation of their neural mechanisms, we engineered humanized GLP1R mouse models, providing an essential platform for *in vivo* studies that would otherwise be unattainable. Through integrated behavioral, neuroanatomical, and functional analyses, we uncovered a previously unknown multi-synaptic hindbrain-amygdala-midbrain circuit that specifically modulates rewarding food consumption through striatal dopaminergic signaling. This discovery advances our understanding of how Glp1R signaling influences not only feeding behavior but also fundamental reward processes, including addiction, mood disorders, and motivation,[7–17,46] highlighting both the therapeutic potential and the need for caution as these treatments see broader use.

Generation and Validation of Humanized Glp1r^{S33W} Mice for Investigating Small-Molecule GLP1RAs

While peptide GLP1RAs, like liraglutide, reduce food consumption in C57BL6J mice, many small-molecule GLP1RAs do not effectively activate rodent Glp1r (**Fig. 1b**) due to a single amino acid difference from tryptophan to serine at position 33 (**Fig. 1c**)[37,38,39]. Using CRISPR-Cas9-mediated genome editing, we inserted the S33W mutation into the mouse *Glp1r* locus, effectively humanizing it (**Fig. 1d,e**). Homozygous humanized Glp1r S33W mice (Glp1r^{S33W}) and wild type (WT) littermates did not exhibit differences in respiratory exchange ratio (RER) (**Extended Data Fig. 1a-d**), energy expenditure (EE) (**Extended Data Fig. 1e-h**) or body weight (**Extended Data Fig. 1i-j**), demonstrating that Glp1r^{S33W} mice maintain normal metabolic functions and energy homeostasis comparable to WT littermates. To evaluate the *in vivo* functionality of the S33W mutation, we performed glucose tolerance tests (GTT) and found that liraglutide improved glucose tolerance in both Glp1r^{S33W} mice and WT mice (**Fig. 1f**), whereas danuglipron and orforglipron were effective only in Glp1r^{S33W} mice (**Fig. 1g,h**). These results demonstrate that Glp1r^{S33W} mice retain responsiveness to peptide-based GLP1RAs while gaining sensitivity to human-specific small molecule GLP1RAs, establishing a valuable *in vivo* model system for investigating this next-generation class of drugs.

Small-Molecule GLP1RAs Mirror Liraglutide Effects in Suppressing Feeding in Glp1r^{S33W} Mice

GLP1RAs induce significant weight loss through multiple mechanisms beyond their effects on insulin secretion and glucose control[1,5,32,47]. To systematically characterize their impact on distinct feeding modalities, we employed parallel behavioral paradigms examining both homeostatic and hedonic feeding patterns. Homeostatic feeding was quantified through standard diet (SD) consumption during the active-phase (zeitgeber time (ZT)12-16), while hedonic feeding was assessed via high-fat diet (HFD) intake during the inactive-phase (ZT2-6) when baseline SD consumption is minimal[48,49,50]. In Glp1r^{S33W} mice, administration of liraglutide, danuglipron, and orforglipron significantly attenuated both active-phase SD (**Fig. 1j,l,n**) and inactive-phase HFD (**Fig. 1p,r,t**) consumption compared to vehicle controls. As predicted by the species specific receptor activation profile, WT mice exhibited reduced SD (**Fig. 1i,k,m**) and HFD (**Fig. 1o,q,s**) intake exclusively following liraglutide administration. Notably, both liraglutide and orforglipron demonstrated sustained 24-hour inhibition of food intake (**Extended Data Fig. 2a-c**), consistent with their extended pharmacokinetic profiles relative to danuglipron (**Fig. 1a**). To validate the clinical relevance of these orally bioavailable small-molecule GLP1RAs, we confirmed that oral danuglipron significantly reduced blood glucose levels (**Fig. 1u**) and acute HFD intake comparable to intraperitoneal injection effects (**Fig. 1v, w**). Similarly, oral orforglipron inhibited acute HFD intake (**Fig. 1x,y**) and its chronic daily administration in overweight Glp1r^{S33W} mice significantly reduced body weight compared to saline controls (**Fig. 1z**), establishing its efficacy in weight management [32] .

GLP1RAs Exhibit Distinct Neural Activation Patterns in Feeding Circuits

Because small-molecule GLP1RAs may have greater brain penetration than large peptide-based GLP1RAs—potentially leading to distinct neural activation patterns—we aimed to identify the brain regions involved in their inhibition of food consumption. First, we focused on nuclei previously reported to be activated by peptide-based GLP1RAs and expressed Glp1r (**Fig. 2a-d**), specifically the dorsomedial hypothalamus (DMH), nucleus tractus solitarius (NTS), area postrema (AP), and central amygdala (CeA)[19,22–24,51–54]. We used cFos expression as a surrogate for GLP1RA-dependent neuronal activation in WT and Glp1r^{S33W} mice treated with danuglipron, orforglipron, and liraglutide (**Fig. 2a-d**). Danuglipron and orforglipron induced significant cFos expression in the NTS (**Fig. 2f**), AP (**Fig. 2g**), and CeA (**Fig. 2h**), but not in the DMH (**Fig. 2e**) of Glp1r^{S33W} mice compared to WT controls, mirroring previous studies using peptide-based GLP1RAs[19,51,55,56]. As expected, liraglutide induced comparable cFos expression in both groups, matching the small-molecule responses in Glp1r^{S33W} mice across all regions, confirming its effective binding to and activation of the Glp1r^{S33W} variant (**Fig. 2e-h**).

Given that activation of the AP is known to induce nausea and malaise, while Glp1R activation in the NTS signals satiation[23,57], we aimed to determine whether the relative cFos activation between these two regions could reveal potential mechanisms underlying the differential effects of GLP1RAs observed in clinical trials[5,32,58,59]. By comparing the ratio of cFos activation in the NTS to that in the AP, we observed significant differences among the drugs tested (**Fig. 2i**). Specifically, orforglipron exhibited greater activation in the NTS and less activation in the AP compared to both danuglipron and liraglutide. To determine whether oral administration of danuglipron replicates the NTS-favored activation pattern observed with orforglipron, we compared intraperitoneal (IP) and oral administration of danuglipron in Glp1r^{S33W} and WT mice (**Fig. 2j,k and Extended Data Fig. 3a-c**). Glp1r^{S33W} NTS cFos activation was comparable

between both routes, but oral delivery significantly reduced AP cFos activation (**Fig. 2l**). These findings indicate that oral danuglipron, its designed route of administration, replicates the NTS-favored activation pattern while minimizing AP activation. This preferential activation is advantageous because it may reduce negative side effects associated with AP activation, such as nausea and malaise, while preserving therapeutic effects mediated by the NTS. Therefore, orally delivered small-molecule GLP1RAs represent a promising advancement in weight loss therapies by enhancing both efficacy and tolerability (**Fig. 1u-y**).

Danuglipron Suppress Food-Motivated Behaviors During Homeostatic and Hedonic Feeding

Building on our observation that peptide-based and small-molecule GLP1RAs produce distinct neuronal activation patterns, we next examined how these differences manifest in the behavior of $Glp1r^{S33W}$ mice. We focused on liraglutide and danuglipron, which share similar pharmacokinetic properties, and monitored mice in a home-cage environment using infrared video over two hours following GLP1RA or vehicle/saline administration in their active phase (ZT12-14) (**Fig. 3a and Extended Data Fig. 4**). By integrating pose estimation (SLEAP[60]) with a probabilistic model for behavior classification (Keypoint-MoSeq[61]), we identified 23 discrete behaviors corroborated by sensor data (**Fig. 3b-d and Extended Data Fig. 5 & 6**). These behaviors were grouped into five principal categories— food-motivated, drinking, resting, moving, and grooming. Principal component analysis (PCA) revealed that both liraglutide and danuglipron induced significant, overall behavioral shifts from control conditions (**Fig. 3e,f and Extended Data Fig. 7a-d**). Specifically, both treatments similarly reduced feeding and drinking while increasing resting-related activity, suggesting a conserved effect on satiety-related behaviors (**Fig. 3g-k**). Linear discriminant analysis (LDA) further supported these findings, clustering the drug-treated groups together and distinctly apart from controls (**Fig. 3l**).

To determine the influence of danuglipron on hedonic feeding, we examined behavioral patterns in SD and HFD-fed mice during the inactive phase (ZT 3-5). Vehicle-treated HFD-fed mice exhibited a behavioral profile distinct from SD-fed mice, with more food-motivated behaviors and drinking, and less resting (**Fig. 3m and Extended Data Fig. 7g-k**), indicating a diet-induced behavioral shift. In contrast, danuglipron-treated HFD-fed mice closely resembled their SD-fed counterparts, showing similar levels of food-motivated activity, drinking, movement, and resting (**Fig. 3m and Extended Data Fig. 7g-k**)). Danuglipron-treated mice on either diet displayed less grooming compared to vehicle-treated counterparts, likely due to reduced food intake naturally shortening the behavioral satiety sequence, which includes a grooming phase following feeding[62]. Together, these findings demonstrate that GLP1RA treatments can realign the behavior of HFD-fed animals toward SD-fed norms (**Fig. 3n and Supplementary Video 1**), effectively neutralizing the behavioral hallmarks of hedonic feeding and reinforcing the notion that distinct neuronal activation patterns translate into meaningful, diet-dependent behavioral outcomes.

Danuglipron Activates Hypothalamic and Hindbrain GLP1R Circuits

To distinguish direct from indirect effects of small-molecule GLP1RAs in specific brain regions, we developed a Cre-dependent adeno-associated virus (AAV) vector expressing full-length human GLP1R (AAV-hSyn-DIO-hGLP1R) (**Fig. 4a**). When applied in Glp1r-Cre mice, this approach enables selective expression of hGLP1R in Glp1r-positive cells, allowing us to isolate

direct activation effects from secondary circuit responses. In Glp1r-Cre mice conditionally expressing hGLP1R in their basomedial hypothalamus (BMH-hGLP1R) (**Extended Data Fig. 8a,b**), danuglipron significantly decreased active-phase SD intake without affecting inactive-phase HFD consumption (**Fig. 4c,h**) while control mice expressing mCherry in the same region showed no changes in consumption (**Fig. 4b,g**). When targeting the DMH, a BMH subnucleus recently implicated in encoding satiation[24,54,63], we found similar selective effects on SD intake (**Fig. 4d,i and Extended Data Fig. 8c,d**). Targeting the hindbrain NTS/AP complex resulted in decreased consumption of both SD and HFD (**Fig. 4e,j and Extended Data Fig. 8e,f**), aligning with recent findings on hindbrain Glp1R circuits in aversion and satiety[23].

Danuglipron Directly Activates CeA^{Glp1r} Neurons to Regulate Hedonic Feeding

Recognizing the limited understanding of the CeA's role in GLP1RA responses[53], we focused our investigation on Glp1r-positive neurons in this region (CeA^{Glp1r}). First, we confirmed CeA^{Glp1r} neurons that conditionally express hGLP1R directly respond to small-molecule GLP1RAs by co-injecting AAV-hSyn-DIO-hGLP1R and AAV-DIO-eYFP into the CeA of Glp1r-Cre mice and performing whole-cell patch-clamp recordings (**Extended Data Fig. 9c-f**). We measured the resting membrane potential of hGLP1R-expressing neurons before and after infusion of 10 μM danuglipron (**Extended Data Fig. 9a**). Consistent with activation of the G_s/cAMP pathway via hGLP1R [64,65], danuglipron elicited significant membrane depolarization, confirming functional expression (**Extended Data Fig. 9b**). Next, to determine whether this responsiveness translates into changes in feeding behavior, we assessed Glp1r-Cre mice conditionally expressing hGLP1R in the CeA (CeA-hGLP1R) under both SD and HFD conditions. Remarkably, CeA-hGLP1R mice showed a selective reduction in inactive-phase HFD consumption without any effect on active-phase SD intake (**Fig. 4f,k and Extended Data Fig. 8g,h**). We corroborated these findings with an alternative virus expressing the small molecule-sensitive mouse SNP, Glp1r^{S33W} and its wildtype control (AAV-DIO-mGlp1r^{S33W} and AAV-DIO-mGlp1r) (**Extended Data Fig. 10a,d**). These results demonstrate that CeA^{Glp1R} neurons selectively modulate hedonic feeding in response to small-molecule GLP1RAs (**Extended Data Fig. 10b,c**), revealing a previously uncharacterized neural substrate for GLP1RA-mediated regulation of feeding behavior.

The relatively small molecular mass of danuglipron (555.6 Da) and its robust effects in CeA-hGLP1R mice suggest this compound can access brain structures beyond the circumventricular organs (CVOs). Although the extent of brain penetration by different GLP1RAs remains an open question[19,51,66,67], definitively establishing their direct engagement of deep nuclear structures is critical for understanding their mechanisms of action. To test whether danuglipron can directly induce neuronal activity in the CeA, we expressed GCaMP7s along with either hGLP1R or mGlp1r in the CeA of Glp1r-Cre mice and recorded calcium transients via fiber photometry *in vivo* (**Fig. 4l and Extended Data Fig. 11a-d**). Since previous work showed peptide-based GLP1RAs induce cFos expression in the CeA of wildtype mice[19,51,55,56]—though whether through direct or indirect pathways remains unclear—we first used liraglutide as a positive control and confirmed it elicited significant calcium transients in CeA-hGLP1R mice (**Extended Data Fig. 11e,f**). Importantly, danuglipron treatment also elicited robust increases in calcium transients in CeA-hGLP1R mice, a response that was absent in mGlp1r-expressing negative controls (**Fig. 4m–p**). These findings provide direct evidence that danuglipron penetrates beyond the CVOs to functionally engage CeA neurons expressing human GLP1R.

Next, we sought to establish the physiological role of CeA^{Glp1R} neurons in hedonic feeding by optogenetically stimulating them independently of any pharmacological agonists and observed

reduced HFD consumption (**Fig. 4q-r**), mirroring the inhibitory feeding effects observed in response to danuglipron in CeA-hGLP1R mice (**Fig. 4k and Extended Data Fig. 10b,c**). To determine whether the CeA is essential for the inhibitory effects of GLP1RAs on feeding, we selectively knocked out Glp1r in the CeA by bilaterally injecting AAV-Cre or AAV-GFP into the CeA of Glp1r$^{flox/flox}$ mice (**Fig. 4s**). Although the loss of CeA Glp1R signaling had no impact on SD intake, it significantly increased HFD consumption following liraglutide injection (**Fig. 4t**). These results pinpoint CeA^{Glp1R} neurons as a critical node in the GLP1RA-responsive circuitry specifically regulating reward-driven feeding behaviors. To further clarify the physiological relevance of this circuit, we asked whether CeA^{Glp1R} neurons receive endogenous GLP-1 input. By expressing synaptophysin in NTS Gcg-Cre neurons, we detected Gcg-positive fibers and synaptic terminals in the CeA (**Fig. 4u**). This demonstrates that CeA^{Glp1R} neurons not only respond to exogenous agonists, but also can receive endogenous GLP-1 signals from the NTS. Together, these findings underscore the CeA as a key integrative hub where GLP-1 signaling—both pharmacologically induced and naturally occurring—converges to curb hedonic feeding[68].

Small-Molecule GLP1RAs Engage CeA to Modulate Mesolimbic Dopamine Release in Response to HFD

Given the selective role of CeA^{Glp1R} neurons in hedonic feeding regulation, we investigated their connectivity to mesolimbic reward circuitry. Anatomical tracing in Glp1r-Cre mice, using AAV-DIO-Synaptophysin or AAV-DIO-eYFP, revealed pronounced projections from CeA-GLP1R neurons to the ventral tegmental area (VTA) (**Fig. 5a and Extended Data Fig. 12a-e**). These findings support a model in which NTS^{Gcg} neurons drive CeA^{Glp1R} activity, which in turn influences VTA neurons and ultimately the nucleus accumbens (NAc) (**Fig. 5b**). Based on our observations that CeA^{Glp1R} activation suppresses hedonic feeding while receptor ablation negates this effect, we hypothesized that these neurons modulate VTA dopaminergic output to reduce NAc dopamine signaling during reward-driven feeding.

To test this hypothesis, we first examined whether GLP1RAs broadly affect dopamine responses in the NAc. By expressing AAV-dLight1.3b in Glp1r^{S33W} mice, we monitored dopamine responses to HFD following peptide (liraglutide) or small-molecule (danuglipron, orforglipron) GLP1RA administration (**Fig. 5c**). Strikingly, all three compounds significantly diminished both the peak and consumption-associated dopamine response (**Fig. 5d–i and Extended Data Fig. 13a-c**), indicating that despite their pharmacological differences, these agents converge on a common central mechanism to reduce dopamine-mediated reward.

To establish a causal link between CeA^{Glp1R} neuron activity and mesolimbic dopamine output, we selectively expressed hGLP1R in the CeA of Glp1r-Cre mice and monitored NAc dopamine dynamics during HFD consumption following danuglipron or orforglipron administration (**Fig. 5j and Extended Data Fig. 12f-h**). Remarkably, both treatments substantially blunted the peak and consumption-associated dopamine responses (**Fig. 5k–p**). This finding demonstrates that activation of GABAergic CeA^{Glp1R} neurons[53] inhibits reward-driven dopamine signaling. By establishing that the CeA-VTA-NAc axis operates in parallel with previously characterized hindbrain to midbrain Glp1R circuits[69–71], our findings reveal a distributed network of Glp1R-expressing neurons orchestrating the suppression of food consumption[23,24,72,73,23,72,74–76].

Discussion

Our findings identify a previously unrecognized amygdalar circuit through which next-generation GLP1RAs modulate reward-driven feeding. In particular, our data indicate that CeA^{Glp1R} neurons receive GLP-1 input from the NTS and influence VTA activity, thereby providing a framework for integrating metabolic signals into dopamine-dependent reward circuits[13,69,74–76]. This insight aligns with an expanding body of evidence that GLP1RAs influence motivational and reward-related processes, raising the possibility of their therapeutic potential for disorders characterized by dysregulated reward, such as substance use[15,16,17,46,77,78]. Looking ahead, our findings raise critical questions about the broader impact of chronic GLP1RA treatment on reward processing. With small-molecule GLP1RAs like orforglipron—described as 'a product for the masses' [31]—gaining traction as accessible, scalable therapies, understanding their long-term effects on brain function becomes essential.

Figures

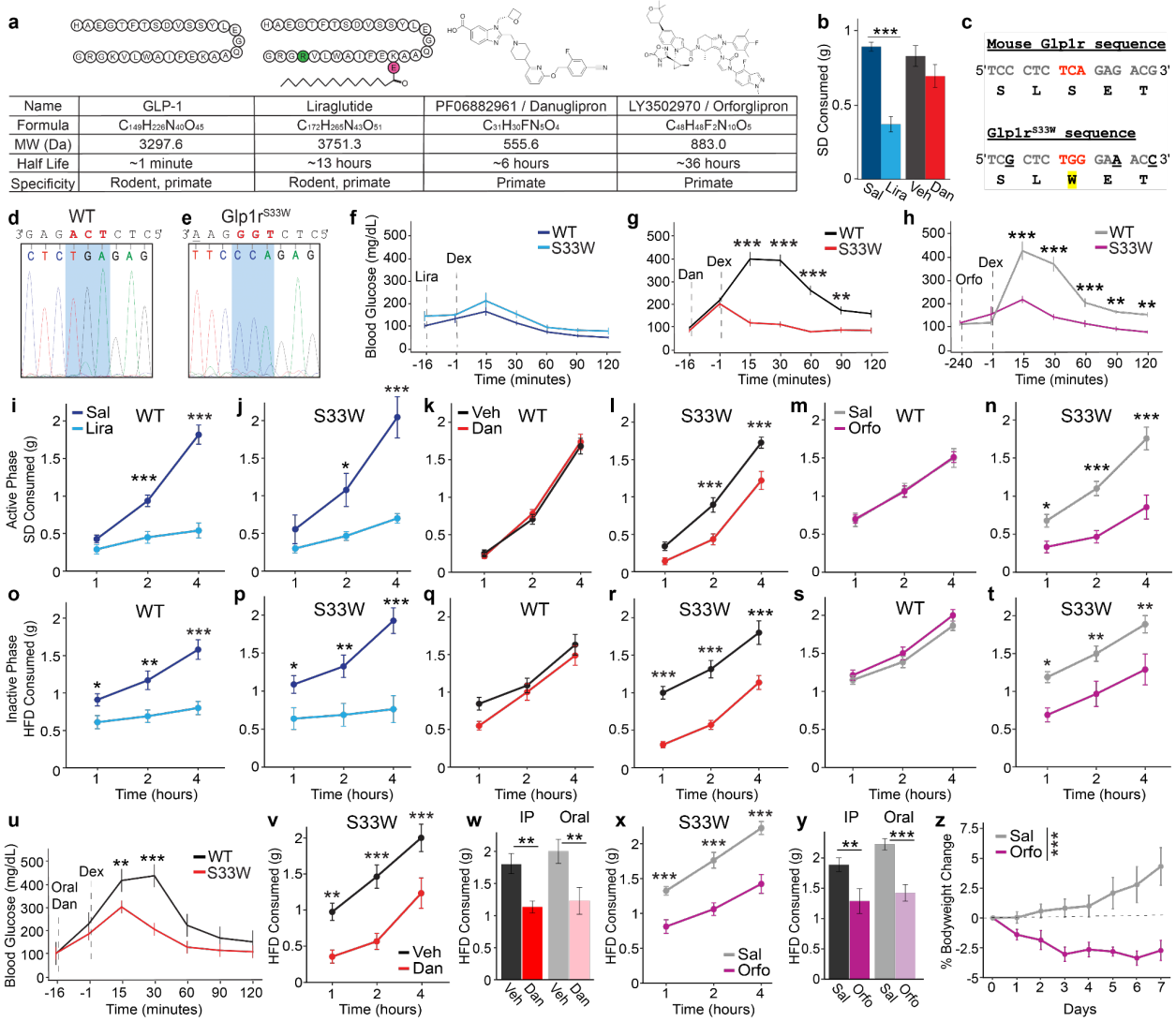

Name	GLP-1	Liraglutide	PF06882961 / Danuglipron	LY3502970 / Orforglipron
Formula	$C_{149}H_{226}N_{40}O_{45}$	$C_{172}H_{265}N_{43}O_{51}$	$C_{31}H_{30}FN_5O_4$	$C_{48}H_{48}F_2N_{10}O_5$
MW (Da)	3297.6	3751.3	555.6	883.0
Half Life	~1 minute	~13 hours	~6 hours	~36 hours
Specificity	Rodent, primate	Rodent, primate	Primate	Primate

Figure 1: Generation and validation of a novel mouse model responsive to small molecule GLP1R agonists: a, Structure, naming convention, molecular formula, molecular weight (MW), half-life in humans, and species binding specificity of glucagon-like peptide-1 (GLP-1), liraglutide, danuglipron, and orforglipron. Amino acid sequences of liraglutide shown with its substitution and additions to GLP-1 highlighted in green and purple, respectively. **b**, Standard diet (SD) consumption over 2 hours post-administration of saline (Sal), liraglutide (Lira), vehicle (Veh), or danuglipron (Dan) (n = 11 per injection, one-way ANOVA with Bonferroni correction, ***P<0.001). **c**, Schematic of the serine (TCA or S) to tryptophan (TGG or W) CRISPR-mediated substitution in Glp1r^{S33W} (bottom) or in mouse Glp1r (top). **d,e**, Sanger sequencing chromatograms of (**d**) WT mouse Glp1r and (**e**) Glp1r^{S33W} sequence, confirming the Glp1r S33W substitution in mice. **f-h**, Glucose tolerance test (GTT) on GLP1RAs. Comparison of blood glucose levels on (**f**) liraglutide (Lira), (**g**) danuglipron (Dan), (**h**) orforglipron (Orfo) followed by dextrose (Dex) in WT and Glp1r^{S33W} mice (n = 5-9 per injection, two-way ANOVA with Bonferroni correction, **P<0.01; ***P<0.001). **i-n**, SD intake 1, 2, and 4 hours post-treatment of (**i, j**) Lira (n = 9-11), (**k, l**) Dan (n

= 15-16), and (**m, n**) Orfo (*n* = 8-9) and vehicle controls in WT and Glp1r^{S33W} mice. **o-t**, High fat diet (HFD) intake 1, 2, and 4 hours post-treatment of (**o, p**) Lira (*n* = 8-10), (**q, r**) Dan (*n* = 14-16), and (**s, t**) Orfo (*n* = 8-9) and their vehicle controls in WT and Glp1r^{S33W} mice (two-way ANOVA with Bonferroni correction, **P*<0.05; ***P*<0.01; ****P*<0.001). **u**, GTT measuring blood glucose levels following oral administration of danuglipron (oDan) and dextrose in Glp1r^{S33W} and WT mice (*n* = 6 per genotype, two-way ANOVA with Bonferroni correction, ***P*<0.01; ****P*<0.001). **v-y**, HFD intake 1, 2, and 4 hours after oral gavage of (**v**) danuglipron or vehicle and (**x**) orforglipron or saline (*n* = 8-9, two-way ANOVA with Bonferroni correction, ***P*<0.01; ****P*<0.001). Comparison of the 4th hour between intraperitoneal (IP) and oral routes of administration with (**w**) danuglipron or (**y**) orforglipron (two-way ANOVA with Bonferroni correction, ***P*<0.01; ****P*<0.001). **z**, 7-day weight changes of mice on chronic HFD treated with orforglipron or saline daily at ZT6 (*n* = 7 per injection, paired t-test, ****P*<0.001). Data are represented as means ± SEM. **P*<0.05; ***P*<0.01; ****P*<0.001. See Supplementary Table 1 for statistical details for all figures and Extended Data figures.

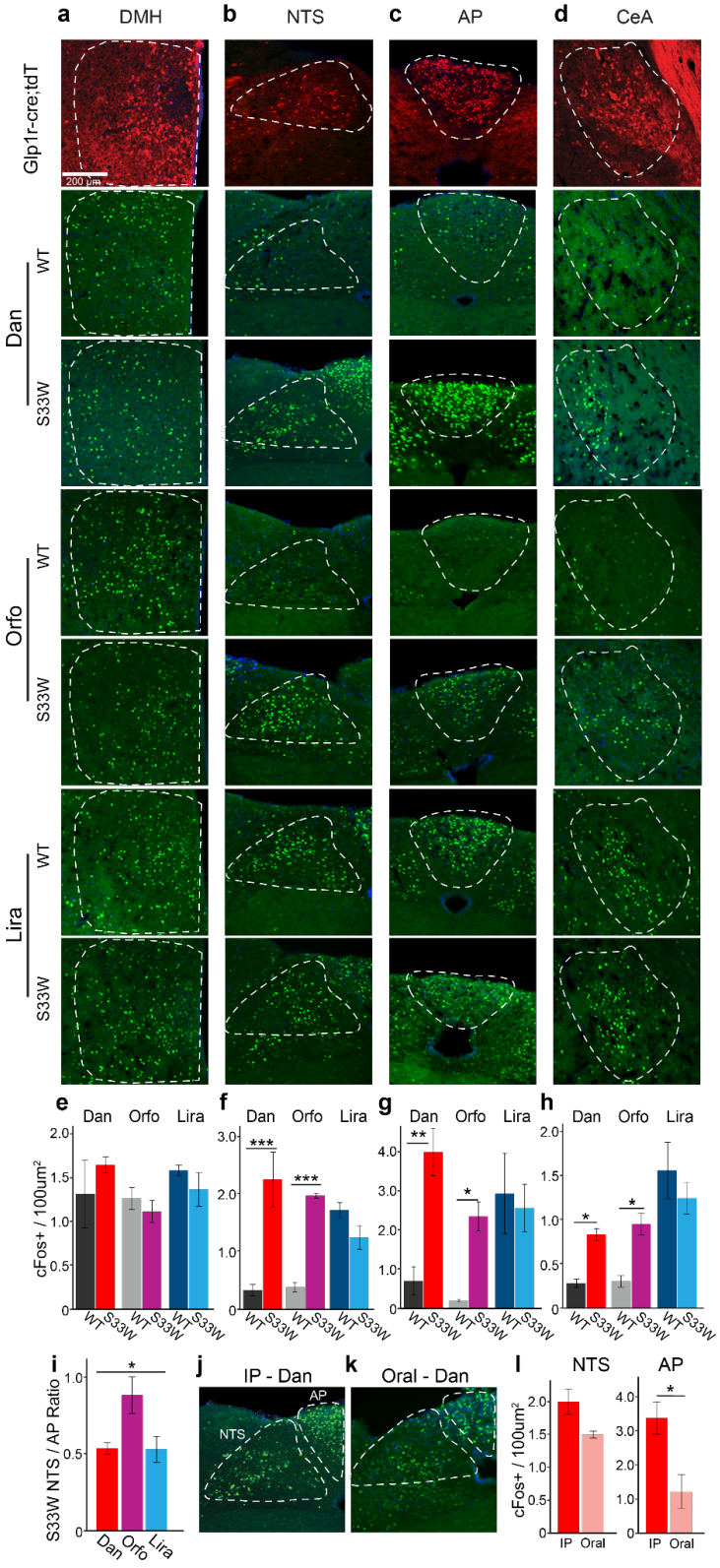

Figure 2: GLP1RA activation across targeted GLP1R-expressing brain regions. **a-d**, GLP1R protein expression validated by a Glp1r-Cre;tdTomato mouse line and neuronal cFos activation 2 hours after danuglipron or liraglutide or 6 hours after orforglipron injection in WT and Glp1r^{S33W}

353 mice in the (**a**) DMH, (**b**) NTS, (**c**) AP, or (**d**) CeA. Scale bars = 200 μm. **e-h**, Quantification of
354 cFos in the (**e**) DMH, (**f**) NTS, (**g**) AP and (**h**) CeA (*n* = 3-4 per genotype, two-way ANOVA with
355 Bonferroni correction, **P*<0.05; ***P*<0.01; ****P*<0.001). **i**, Ratio of NTS/AP cFos activation in
356 Glp1r^{S33W} mice after danuglipron, orforglipron, and liraglutide (*n* = 3-4 per injection, Kruskal-Wallis
357 test, **P*<0.05). **j,k**, Neuronal cFos activation in the NTS and AP 2 hours after danuglipron was
358 administered to Glp1r^{S33W} mice via (**j**) IP injection or (**k**) oral gavage. **l**, Quantification of cFos
359 expression in the NTS (left) or AP (right) following danuglipron IP or oral delivery in Glp1r^{S33W} mice
360 (*n* = 3 per delivery route, Welch's t-test, **P*<0.05). Data are represented as means ± SEM.
361 **P*<0.05; ***P*<0.01; ****P*<0.001.
362
363
364
365
366
367
368

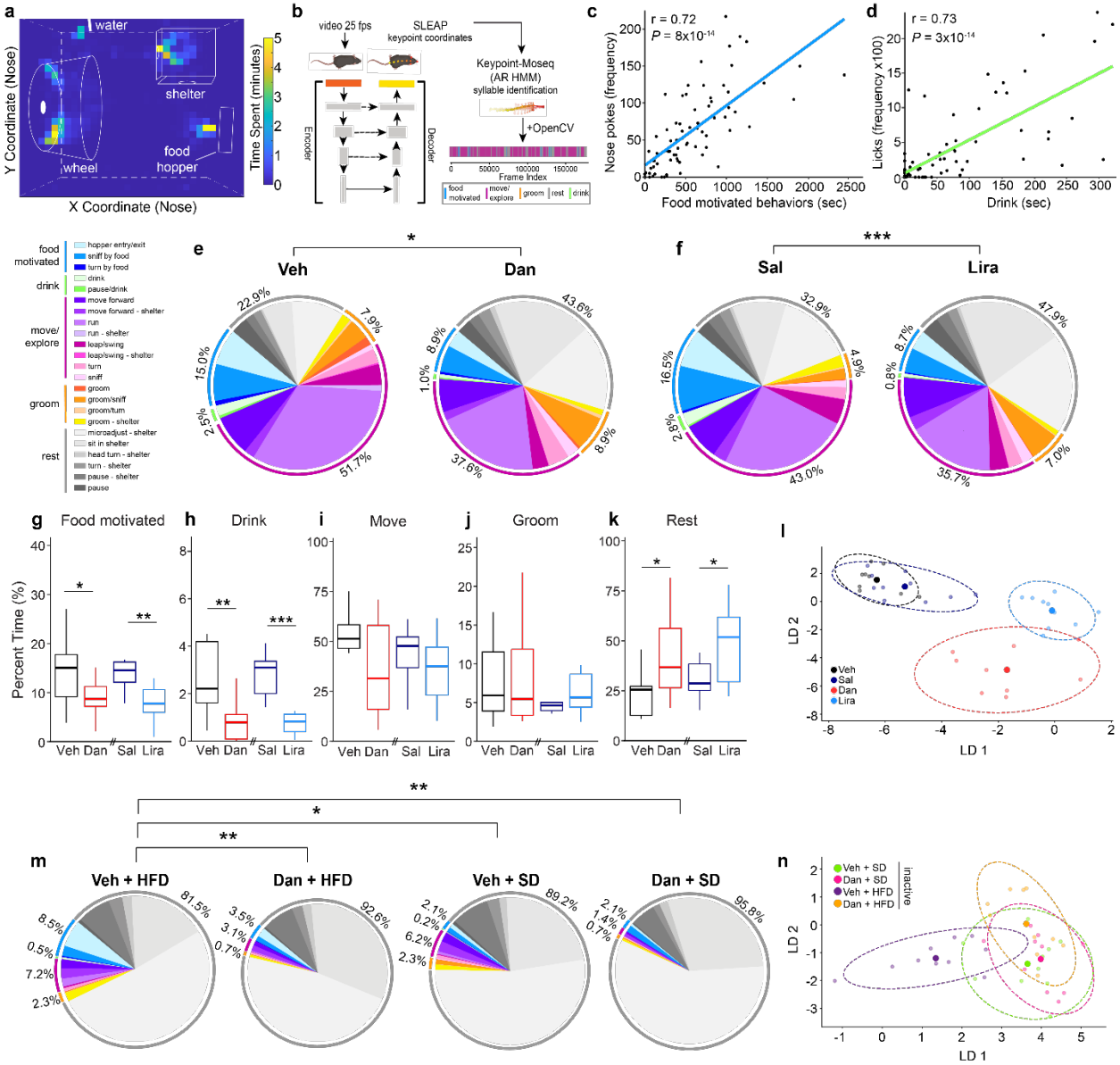

Figure 3: Machine-learning assisted behavior profiling reveals distinct phenotypes associated with GLP1RA and diet. a, Representative heatmap of Glp1r^{S33W} mouse nose location and home cage setup. Color indicates time spent in minutes over 2 hours. **b,** Simplified pipeline for machine learning analysis of behavior[60,61]. Analysis parameters: SLEAP tracking with 9 keypoints at 25 fps, Keypoint-MoSeq fit an autoregressive hidden Markov model (AR-HMM) to PCA-reduced keypoints. A full model was then trained, producing 91 behavioral syllables with a minimum frequency threshold of ≥0.01%. Trained raters manually named behaviors, incorporating locational context via OpenCV. **c,d**, Correlation between sensor data and video analysis across all conditions tested for (**c**) food hopper nose pokes and food motivated behaviors and (**d**) water bottle spout licks and drinking (n = 78, Pearson regression, ***P<0.0001). **e,f**, Proportion of time spent performing each of the 23 behaviors identified using Keypoint-MoSeq and averaged across all mice per condition, binned into 5 behavior categories. A MANOVA was run on the PCA of the proportion of time spent performing each behavioral category. PCA was ran for (**e**) Veh and Dan and (**f**) Saline and Lira (n = 9 Veh/Dan, n = 10 Sal/ Lira, RM MANOVA with resampling MATS,

*P<0.05, ***P<0.001). **g-k**, Percentage of time spent (**g**) food seeking, (**h**) drinking, (**i**) moving/exploring, (**j**) grooming, and (**k**) resting. (n = 9 Veh/Dan, n = 10 Sal/Lira, generalized linear mixed-effects model with beta regression, *P<0.05, **P<0.01, ***P<0.001). **l,** Linear discriminant analysis (LDA) plot of the similarity between mean behavioral summaries of mice per condition. Opaque centroid circles represent the mean behavioral summaries per condition, small circles indicate the specific embedding locations of individual mice within each condition, and ellipses denote two standard deviations from the mean for each group. **m,** Proportion of time spent performing each of the 23 behaviors, and 5 larger behavioral categories in SD- and HFD-fed mice during the light cycle after vehicle or danuglipron. MANOVA was run on PCA of the 23 behavior durations (n = 10, RM MANOVA with resampling MATS and holm correction, *P<0.05, **P<0.01). **n,** LDA plot of the similarity between mean behavioral summaries of mice per condition. Data are represented as medians ± Q1-Q3. *P<0.05; **P<0.01; ***P<0.001.

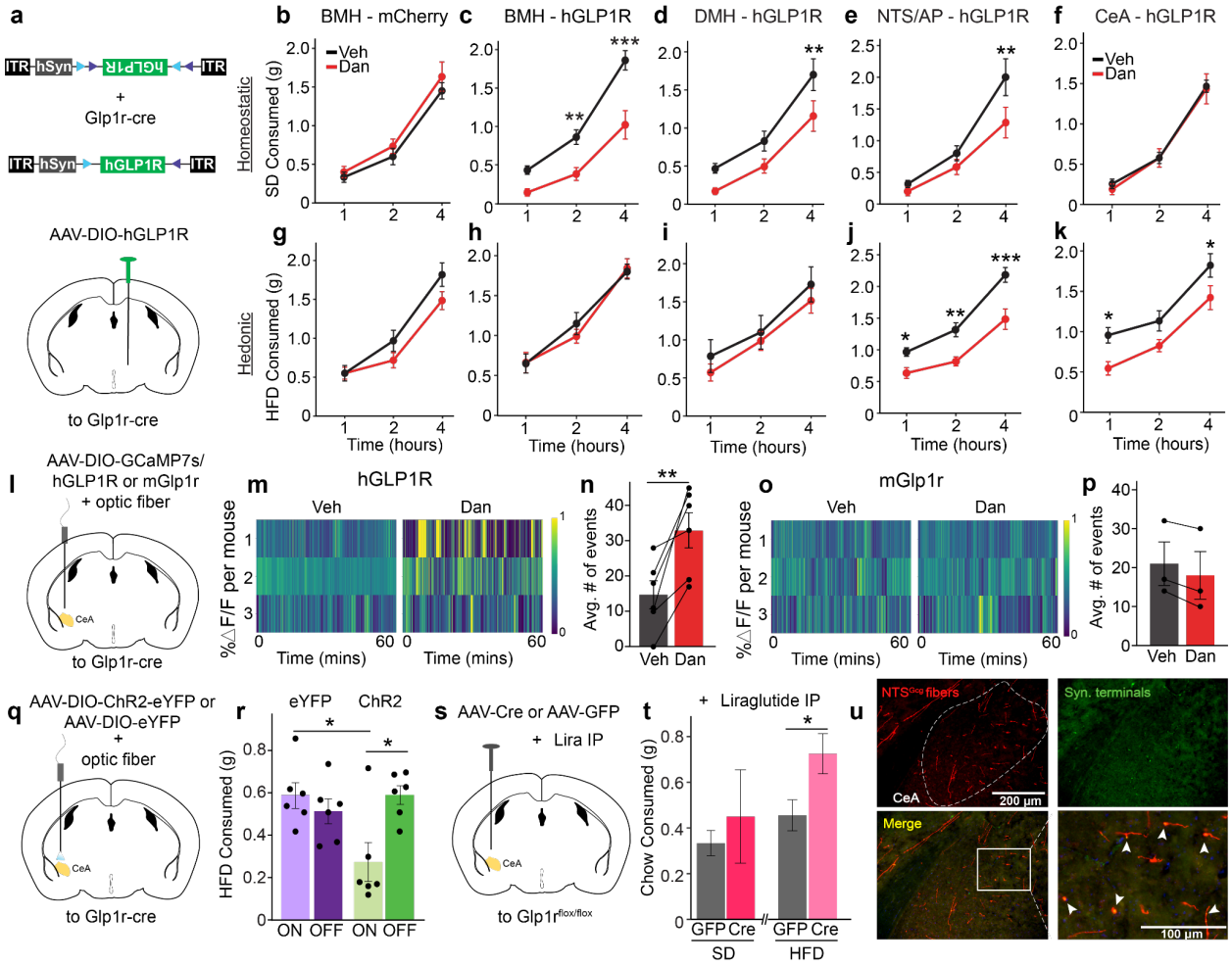

Figure 4: Central amygdala GLP1R activation inhibits hedonic food intake via direct activation by danuglipron. a, Representative schematic of AAV-DIO-hGLP1R viral construct and injection into the basomedial hypothalamus (BMH). **b-k**, 1, 2, and 4-hour SD or HFD consumption after vehicle (Veh) or danuglipron (Dan) in Glp1r-Cre mice expressing (**b,g**) AAV-DIO-mCherry (BMH-mCherry, *n* = 6) or (**c,h**) AAV-DIO-hGLP1R (BMH-hGLP1R, *n* = 10) in the BMH, (**d,i**) DMH (*n* = 7), (**e,j**) NTS/AP (*n* = 6), or (**f,k**) CeA (*n* = 9) (two-way ANOVA with Bonferroni correction, **P*<0.05; ***P*<0.01; ****P*<0.001). **l,** Schematic of AAV-DIO-GCaMP7s + AAV-DIO-hGLP1R or mGLP1R injection with a fiber optic implant to the CeA of Glp1r-Cre mice. **m-p,** Representative heatmaps of %ΔF/F neuronal calcium signal per mouse during 1-hour of fiber photometry recording after vehicle or danuglipron injection in (**m**) hGLP1R or (**o**) mGLP1R expressing mice. Number of significant calcium events averaged per mouse during 1-hour recording session following vehicle or danuglipron in (**n**) hGLP1R or (**p**) mGLP1R expressing mice (*n* = 3-6 per injection, paired t-test, ***P*<0.01 and Wilcoxon signed-rank test). **q,** Schematic of AAV-DIO-eYFP or AAV-DIO-ChR2-eYFP injection with a fiber optic implant to the CeA of Glp1r-Cre mice. **r,** 30-minute HFD consumption in ChR2 and eYFP expressing controls after 20 Hz blue light stimulation (ON) or no stimulation (OFF) (*n* = 6 per group, two-way ANOVA with Tukey's HSD correction, **P*<0.05). **s**, Schematic of AAV-Cre to conditionally knockout Glp1r, or AAV-GFP control injection to the CeA of Glp1r$^{flox/flox}$ mice. **t**, SD (left) and HFD (right) consumption 4 hours after injection of liraglutide in AAV-Cre or AAV-GFP expressing mice. (*n* = 6, Welch's t-test, **P*<0.05). **u**, Representative images of the CeA from Gcg-Cre mice injected with AAV-DIO-mGFP-

2A-Synaptophysin-mRuby in the NTS; scale bar = 200 μm. NTS^{GCG} fibers (red; pseudo-colored mGFP; top left), synaptic terminals (green; pseudo-colored mRuby; top right) are shown, with a magnified view (bottom right; scale bar = 100 μm). Data are represented as means ± SEM. *P<0.05; **P<0.01; ***P<0.001.

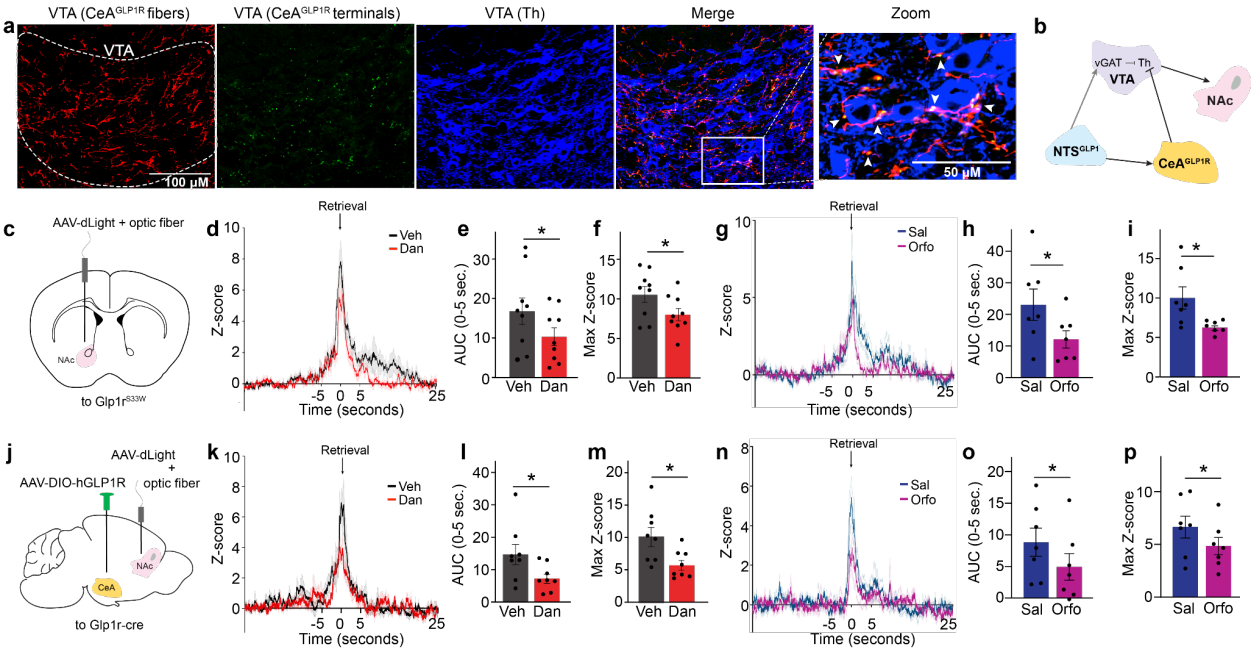

Figure 5: CeA^{GLP1R} neurons project to the VTA to modulate dopamine output to the NAc in response to HFD. a, Representative image of the VTA from Glp1r-Cre mice injected with AAV-DIO- mGFP-2A-Synaptophysin-mRuby in the CeA; scale bar = 100 µm. CeA^{GLP1R} fibers (red; pseudo-colored mGFP), synaptic terminals (green; pseudo-colored mRuby), and tyrosine hydroxylase-positive neurons (Th; blue, marking dopaminergic neurons) are shown, with a magnified view (right; scale bar = 50 µm). **b**, Schematic of proposed neural circuit from NTS → CeA → VTA → NAc. Arrows indicate neuron activation, blunted ends indicate neuron inhibition. Gray arrow from NTS → VTA indicates a known connection from NTS^{GLP-1} to VTA^{vGAT} neurons [71]. **c**, Schematic of genetically-encoded dopamine sensor, AAV-dLight1.3b, injection and fiber optic implant in the NAc of Glp1r^{S33W} mice. **d,g**, Averaged Z-score traces showing dopamine release in the NAc in response to HFD following administration of (**d**) vehicle or danuglipron and (**g**) saline or orforglipron in Glp1r^{S33W} mice. Traces are aligned to food retrieval time (t = 0) and averaged across five food trials per mouse. **e-i**, Quantified (**e,h**) area under the curve (AUC) for Z-scores and (**f,i**) maximum fluorescence Z-scores within the food retrieval window (n = 9 for danuglipron, n = 7 for orforglipron, paired t-test, *P<0.05). **j**, Schematic of AAV-dLight1.3b injection and fiber optic implant into the NAc and AAV-DIO-hGLP1R injection into the CeA of Glp1r-Cre mice. **k,n**, Averaged Z-score traces showing dopamine release in the NAc in response to HFD following administration of (**k**) vehicle or danuglipron and (**n**) saline or orforglipron in CeA-hGLP1R mice. Traces are aligned to food retrieval time (t = 0) and averaged across five food trials per mouse. **l-p**, Quantification of (**l,o**) AUC for Z-scores and (**m,p**) maximum fluorescence Z-scores within the food retrieval window (n = 8 for danuglipron, n = 7 for orforglipron, paired t-test, *P<0.05). Data are represented as means ± SEM. *P<0.05; **P<0.01; ***P<0.001.

Methods

Mouse lines

All experiments were carried out in compliance with the Association for Assessment of Laboratory Animal Care policies and approved by the University of Virginia Animal Care and Use Committee. Mice were housed on a 12:12-hour light/dark (LD) cycle with food (PicoLab Rodent Diet 5053) and water *ad libitum* unless otherwise indicated. For experiments, we used 8-week or older male and female C57BL6/J mice, Glp1r-IRES-Cre mice (Glp1rtm1.1(cre)Lbrl/RcngJ, strain #029283, RRID:IMSR_JAX:029283), Glp1r-IRES-Cre mice crossed to Ai14 tdTomato reporter line (B6.Cg-Gt(ROSA)26Sortm14(CAG-tdTomato)Hze/J, strain #007914, RRID:IMSR_JAX:007914), Glp1r$^{flox/flox}$ mice (B6(SJL)-Glp1rtm1.1Stof/J, strain #035238, RRID:IMSR_JAX:035238), Gcg-Cre mice (C57BL/6J-Tg(Gcg-cre)-1Mmsc/Mmmh, stock #051056-MU, RRID:MMRRC_051056-MU) and Glp1r^{S33W} mice (described below). Gcg-Cre mice were rederived by *in vitro* fertilization from frozen sperm (MMRRC, stock no. 051056-MU).

Generation of Glp1r^{S33W} mouse

The Glp1r^{S33W} mouse line was created with CRISPR-Cas9 homologous repair at the University of Virginia Genetically Engineered Murine Model Core. Briefly, Cas-9 (Alt-R™ S.p. Cas9 Nuclease V3, 100 µg, catalog no. 1081058), Alt-R™ HDR Donor Oligo repair template (below), tracrRNA (Alt-R® CRISPR-Cas9 tracrRNA, 5 nmol, catalog no. 1072532), and CRISPR-Cas9 crRNA XT (ATTTCTGCACCGTCTCTGAG) were microinjected into a fertilized B6SJL zygote and were implanted into a pseudopregnant female. Founder pups were genotyped as described below and backcrossed to C57BL6/J mice for at least 4 generations before experimentation.

Repair Template

aagagggtgggagtccagtgggaccagaggggctgctggagccacggggcttctgcttttatttctgctttcccttgtagGGTACCA
CGGTG**TCGCTC<u>TGG</u>GAAACCGTCCAAAAGTGG**AGAGAATACCGGCGGCAGTGCCAGCGT
TTCCTCACGGAAGCGCCACTCCTGGCCACAGgtgcgtccagatgaggcctcacg

Validating Glp1r^{S33W} mice

Tail snips were obtained from pups at 3 weeks of age. DNA was extracted with an extraction buffer (Sigma, catalog no. E7526) and tissue prep solution (Sigma, catalog no. T3073), heated for 10 and 3 minutes at 55°C and 100°C, respectively, then neutralized with a neutralization solution (Sigma, catalog no. N3910). PrimeSTAR High Fidelity PCR (Takara, catalog no. R050A) was performed with 1uL of cDNA and 10uM of 5′-3′ F (GATCCCCAAAGTGGCAGTCA) and 5′-3′ R (AGCTATGGACTGGGGATCGT) primers. After amplification, the PCR product was run on a 1.2% agarose gel and bands were cut out at 330 bp. DNA was gel extracted and purified (Qiagen, catalog no. 28704), mixed with 5uM right primer, H_2O, and subsequently sent to be analyzed via Sanger sequencing (Azenta). Chromatogram results were analyzed to assign wild type, heterozygous, or homozygous genotypes for each mouse.

Generation of GLP1R viruses

The full length human *Glp1r* gene was obtained by PCR, amplifying the human fragment from GLP1R-tango (plasmid from Addgene, #66295, RRID:Addgene_66295), including the leader sequence present in the GLP1R-tango. The primers used were: 5′-3′ F (AAAGCT-AGCGCCACCATGAAGACGATCATCGCCCTGAGC) and 5′-3′ R (TTTGGCGCGCCCTAA-GAGCAGGACGCCTGACAAGT), ligating the product into pAAV-hSyn-DIO-EGFP (plasmid from Addgene, #50457, RRID:Addgene_50457) in place of the EGFP in NheI and AscI sites to produce the human GLP1R virus construct (AAV-hSyn-DIO-hGLP1R). The full length mouse *Glp1r* wild type gene was synthesized by Twist Biosciences (USA), generating a NheI and AscI fragment. This construct included the same leader sequence present in the human construct, as well as an

HA-tag encoded at the C-terminus of the full length mouse protein coding region. The fragment was inserted into pAAV-hSyn-DIO-EGFP (plasmid from Addgene, #50457, RRID:Addgene_50457) in place of EGFP to produce the plasmid construct (AAV-hSyn-DIO-mGLP1R-HA). The full length mouse *Glp1r* gene bearing a Ser to Trp mutation at position 33 (S33W) was made by inserting a synthetic NheI and StuI fragment prepared by Twist Biosciences, containing the single mutation within this fragment. This was cloned into the sites present in the wild type construct to produce the S33W mouse mutant, followed by an HA-tag encoded at the C-terminus (AAV-hSyn-DIO-mGLP1R^{S33W}-HA). Viral plasmid constructs were confirmed by Sanger sequencing. Virus plasmid constructs were prepared and sent to the University of North Carolina Viral Core (Chapel Hill, NC) for preparation of the AAV (serotype 8).

Stereotactic surgery

Mice were anesthetized with isoflurane (5% induction and 2 to 2.5% maintenance; Isothesia) and placed in a stereotaxic apparatus (AWD). A heating pad was used for the duration of the surgery to maintain body temperature, and ocular lubricant was applied to the eyes to prevent desiccation. A total of 200-400 nL was microinjected per side of [rAAV8/AAV2-hSyn-DIO-hGLP1R, plasmid from Addgene, virus packed at UNC GTC Vector Core, Lot #AV9862 (100 µL at titer ≥ 1.5 ×10^{13} vg/mL); AAV8-hSyn-DIO-mGLP1R^{S33W}-HA, synthesized by Twist Biosciences, virus packed at UNC GTC Vector Core, Lot #AV10104 (100 µL at titer ≥ 8.2×10^{12} vg/mL); AAV8-hSyn-DIO-mGLP1R-HA, synthesized by Twist Biosciences, virus packed at UNC GTC Vector Core, Lot #AV10103 (100 µL at titer ≥ 4.5×10^{12} vg/mL); pAAV9-syn-dLight1.3b, plasmid from Addgene, #135762, RRID:Addgene_135762, virus packed at UNC GTC Vector Core (100 µL at titer ≥ 1.5×10^{13} vg/mL); pAAV1-EF1a-DIO- hChR2(H134R)-EYFP-WPRE-HGHpA, plasmid from Addgene, #20298, RRID:Addgene_20298, virus packed at UNC GTC Vector Core (100 µL at titer ≥ 7×10^{12} vg/mL); pGP-AAV1-syn-DIO-jGCaMP7s-WPRE, plasmid from Addgene, #104491, RRID: Addgene_104491, virus packed at UNC GTC Vector Core (100 µL at titer ≥ 1×10^{13} vg/mL); pAAV1-Ef1a-DIO-EYFP, plasmid from Addgene, #27056, RRID:Addgene_27056, virus packed at UNC GTC Vector Core (100 µL at titer ≥ 1×10^{13} vg/mL); AAV8-hSyn-DIO-mCherry, plasmid from Addgene #50459, RRID:Addgene_50459, and virus packed at UNC Vector Core (100 µL at titer ≥ 7×10^{12} vg/mL); pAAV-hSyn-FLEx-mGFP-2A-Synaptophysin-mRuby, plasmid from Addgene, #71760, RRID:Addgene_71760, and virus packed at UNC Vector Core; pENN.AAV.hSyn.HI.eGFP-Cre.WPRE.SV40, plasmid from Addgene, #105540-AAV8, RRID:Addgene_105540-AAV8, and virus packed at UNC Vector Core (100 µL at titer ≥ 1×10^{13} vg/mL); pAAV-hSyn-EGFP, plasmid from Addgene, #50465-AAV8, RRID:Addgene_50465-AAV8, and virus packed at UNC Vector Core (100 µL at titer ≥ 7×10^{12} vg/mL)], plasmid was delivered using a glass pipette at a flow rate of 50 nl/min driven by a microsyringe pump controller (World Precision Instruments, model Micro 4). The syringe needle was left in place for 10 min and was completely withdrawn 17 min after viral delivery. For *in vivo* calcium and dopamine imaging and optogenetics, a unilateral fiber optic cannula (RWD, Ceramic Ferrule, Ø400-µm, 0.5 numerical aperture) was implanted 0.2-mm dorsal to the viral injection coordinates following viral delivery and stabilized on the skull with dental cement (C&B METABOND, Parkell). Two weeks minimum were allowed for recovery and transgene expression after surgery. Stereotaxic coordinates relative to Bregma (George Paxinos and Keith B. J. Franklin): basomedial hypothalamus, mediolateral (ML): ±0.3 mm, anterior posterior (AP): −1.4 mm, dorsoventral (DV): −5.9 mm; DMH, ML: ±0.3 mm, AP: −1.8 mm, DV: −5.4 mm; CeA, ML: ±2.7 mm, AP: −1.3 mm, DV: −4.6 mm; VTA, ML: ±0.5 mm, AP: −3.6 mm, DV: −4.5 mm; NAc, ML: ±1.25 mm, AP: +1.0 mm, DV: −4.7 mm from Bregma; and NTS/AP, ML: ± 0.15 mm, AP: −0.3 mm, DV: −0.1, −0.4 mm from the Zero point of the calamus scriptorius. All surgical procedures were performed under sterile conditions and in accordance with University of Virginia Institutional Animal Care and Use Committee guidelines. Histological analysis was performed to validate the success of intracranial surgeries. Mice with unsuccessful viral/implant targeting were excluded.

563
564 **GLP1R agonists**
565 Liraglutide powder (Selleck, catalog no. S8256) was dissolved in 0.9% NaCl sterile saline, lightly
566 sonicated, and further diluted in 0.9% NaCl sterile saline to 0.03mg/mL. Danuglipron powder
567 (Selleck, catalog no. S9851) was dissolved to 30 mg/mL in 100% ethanol with gentle sonication,
568 then diluted to 3mg/mL (food intake) or 0.3mg/mL (GTT) in vehicle [1N NaOH, 2% Tween 80, 5%
569 polyethylene glycol (PEG) 400, 5% dextrose][35]. Orforglipron powder (MedChemExpress, catalog
570 no. HY-112185) was dissolved to 10mg/mL in Dimethyl sulfoxide (DMSO) and further diluted in
571 0.9% NaCl sterile saline to 0.1mg/mL.
572
573 **Histological analysis and imaging**
574 For fixed tissue collection, mice were deeply anesthetized (ketamine:xylazine, 280:80 mg/kg,
575 intraperitoneally) and perfused intracardially with ice-cold 0.01M phosphate buffer solution (PBS),
576 followed by fixative solution [4% paraformaldehyde (PFA) in PBS at a pH of 7.4]. For testing brain
577 region cFos activation (Fig. 3), danuglipron (30 mg/kg), orforglipron (1 mg/kg), or liraglutide (0.3
578 mg/kg) was delivered via intraperitoneal injection or oral gavage 2 hours (or 6 hours for
579 orforglipron) before perfusion and brain harvesting. After perfusion, brains were harvested and
580 postfixed overnight at 4°C in PFA. Fixed brains were then transferred into 30% sucrose in PBS
581 for 24 hours and then frozen on dry ice. Frozen brains were sectioned immediately or stored in
582 −80°C for future processing. Coronal sections (30 μm) were collected with a cryostat (Microm HM
583 505 E). Sections were permeabilized with 0.3% Triton X-100 in PBS (PBS-T) and blocked with
584 3% normal donkey serum (Jackson ImmunoResearch, RRID:AB_2337258) in PBS-T (PBS-T DS)
585 for 30 min at room temperature. Sections were then incubated overnight at room temperature in
586 primary antibodies diluted in PBS-T DS. For visualization, sections were washed with PBS-T and
587 incubated with appropriate secondary antibodies diluted in the PBS-T DS for 2 hours at room
588 temperature. Sections were washed three times with PBS and mounted using DAPI Fluoromount-
589 G (Southern Biotech, catalog no. 0100-20). Images were captured on a Zeiss Axioplan 2 Imaging
590 microscope equipped with an AxioCam MRm camera using AxioVision 4.6 software (Zeiss) or
591 confocal microscope imaging was performed on a Zeiss LSM 800 microscope (Carl Zeiss). The
592 following primary antibodies were used for fluorescent labeling: anti-c-Fos (rabbit, 1:1000;
593 Synaptic Systems, #226003, RRID:AB_2231974), anti-DsRed (rabbit, 1:1000; Takara Bio,
594 catalog no. 632496, RRID:AB_10013483), anti-TdTomato (goat, 1:1000; Arigobio, catalog no.
595 ARG55724), anti-hGLP1R (rabbit, 1:200; Invitrogen, catalog no. PA5-97789, RRID:
596 AB_2812404), anti-HA (rabbit, 1:1000, Cell Signaling, catalog no. 3724), anti-Th (rabbit, 1:500;
597 Chemicon, catalog no. AB152), and anti-GFP (goat, 1:500; Rockland, catalog no. 600-101-215).
598 The secondary antibodies (Jackson ImmunoResearch) used were Cy2-conjugated donkey anti-
599 rabbit (1:250; catalog no. 711-225-152, RRID:AB_2340612), Cy3-conjugated donkey anti-rabbit
600 (1:250; catalog no. 711-165-152, RRID:AB_2307443), Cy5-conjugated donkey anti-rabbit (1:250;
601 catalog no. 711-175-152, RRID:AB_2340607), Cy3-conjugated donkey anti-goat (1:250; catalog
602 no. 705-165-147, RRID:AB_2307351), and Alexa-Fluor® 488 donkey anti-goat (1:250; catalog
603 no. 705-545-003, RRID:AB_2340428).
604
605 **Antigen retrieval for hGLP1R staining**
606 Antigen retrieval was performed before immunohistochemistry staining of human GLP1R, by
607 incubating the sections in the following solutions sequentially in room temperature: 1% NaOH +
608 0.3% H_2O_2 in PBS for 20 min, 0.3% glycine in PBS for 10 min, and 0.03% sodium dodecyl sulfate
609 (SDS) in PBS for 10 min. Then, antigen retrieval–treated sections were stained following the
610 immunohistochemistry staining procedures described.
611
612
613

614 **Fos analysis pipeline**
615 Fos images were uploaded to ImageJ (FIJI) and cropped based on brain regions outlined in the
616 Allen Brain Atlas. The area of the cropped regions were measured and recorded. Image
617 thresholds were set per image and particles were analyzed within the size restriction of 50-500
618 pixels. cFos particles were analyzed per image, and total particles of each image were divided by
619 total area of the image. At least three cFos images per region for each mouse was quantified and
620 averaged per mouse and per genotype (WT or Glp1r^{S33W}). Ratios of NTS/AP Fos activation in
621 Glp1r^{S33W} mice were calculated by dividing Fos/area of NTS over AP for each mouse and
622 averaged per injection.
623
624
625 **<u>Behavioral Assays</u>**
626
627 **Metabolic analysis in comprehensive lab animal monitoring system**
628 Indirect calorimetry in the comprehensive lab animal monitoring system (CLAMS, Columbus
629 Instruments) was used to evaluate metabolic parameters of WT and Glp1r^{S33W} mice. All WT and
630 Glp1r^{S33W} mice were single housed and maintained on a 12:12-hour LD cycle with *ad libitum*
631 access to food (PicoLab Rodent Diet 5053) and water. Metabolic measures of respiratory
632 exchange ratio and energy expenditure were averaged over 3 days per mouse and per genotype.
633 (n = 10/11 mice per genotype). Averaged LD cycle and total 24 hour respiratory exchange ratio
634 and energy expenditure was analyzed per genotype and per sex.
635
636 **Glucose tolerance tests**
637 WT or Glp1r^{S33W} mice were overnight fasted for 16 hours prior to experiment start (zeitgeber time
638 [ZT] 10 - ZT2). Mice received a tail snip and blood glucose measure using a Glucometer
639 (OneTouch Ultra Test Strips for Diabetes), along with injection or oral gavage of danuglipron
640 (3mg/kg) or liraglutide (0.3mg/kg) 15 minutes prior to dextrose (D-glucose) injection, or
641 orforglipron (1mg/kg) 240 minutes prior to dextrose. At time point 0, mice received a blood glucose
642 measure and injection of dextrose (1g/kg). At 15, 30, 60, 90, and 120 minutes after injection, blood
643 glucose levels were measured.
644
645 **Homeostatic food intake**
646 Home cages were changed and food was removed from the home cage 1 hour prior to experiment
647 start. Mice were injected with vehicle/saline or drug (danuglipron 30mg/kg, liraglutide 0.3mg/kg,
648 orforglipron 1mg/kg) at ZT11.5 (ZT8 for orforglipron) and two pellets of standard diet (PicoLab
649 Rodent Diet 5053) were placed on the home cage floor at ZT12. Food intake measurements were
650 taken at 1, 2, and 4 hours after ZT12 using infrared night vision goggles (Nightfox Swift Night
651 Vision Goggles).
652
653 **Hedonic food intake**
654 Mice were habituated to high fat diet (HFD; Open Source, D12451; 4.73 kcal/gram; 45% fat, 20%
655 protein, 35% carbohydrates; 17% sucrose) for 1 hour over two days before testing days. Standard
656 diet was removed from the home cage 1 hour prior to experiment start. Mice were injected with
657 vehicle/saline or drug (danuglipron 30mg/kg, liraglutide 0.3mg/kg, orforglipron 1mg/kg) at ZT1.5
658 and one pellet of HFD was placed on the home cage floor at ZT2 (ZT5.5 for orforglipron). Food
659 intake measurements were taken at 1, 2, and 4 hours after HFD delivery. The same parameters
660 were used in oral gavage experiments with danuglipron and orforglipron
661
662 **Optogenetic Food Intake Analysis**
663 Mice were single-housed for at least five days and habituated to a fiber optic cable and high fat
664 diet for one hour over two days. On the test day, home cages were changed and food was

removed 1 hour prior to the start of the experiment. During the test day, a pre-measured pellet of high-fat diet (HFD) was provided to each mouse. The test paradigm was 30 minutes of laser stimulation followed by 30 minutes without laser stimulation. Food intake during each 30-minute interval was measured. The laser stimulation protocol was 20 Hz, 473 nm blue light with a 2-second on and 3-second off pattern. The light power exiting the fiber optic cable, measured using an optical power meter (Thorlabs), was maintained at 7-8 mW across all experiments. Experiment performed during the light phase, between ZT3-ZT4. Mice with missed virus injection or off-target fiber placement were excluded from analysis.

Weight loss experiment

Male Glp1r^{S33W} mice >8 weeks old were placed on a high fat diet (Open Source, D12451; 4.73 kcal/gram; 45% fat, 20% protein, 35% carbohydrates; 17% sucrose) for at least 8 weeks prior to experiment start. Mice that did not gain at least 20% of their baseline body weight were excluded from testing. Mice were randomly assigned to saline or orforglipron (1mg/kg) injection groups and retested with the opposite treatment after a week of rest. Glp1r^{S33W} mice were injected daily at ZT6 and food and body weight were measured.

Home cage monitoring of Glp1r^{S33W} mice

Mice were singly housed and acclimated to home cage PhenoTyper boxes (Noldus, Netherlands) for 5 days prior to testing. The cages were maintained on a 12:12-hour light-dark (LD) cycle. During the acclimation period, mice had *ad libitum* access to standard diet (SD) provided in a food hopper, along with water bottles, running wheels, shelters, and bedding. Mice that failed to meet a baseline threshold of food hopper activity (<50 nose pokes from ZT 12-14) after habituation were excluded from the study to ensure sufficient engagement with the feeding setup. Of the 38 mice tested, 9 did not meet this criterion and were excluded. For the light cycle experiment, mice were additionally habituated to high-fat diet (HFD) for 2 days prior to testing. For testing, danuglipron (30 mg/kg) or vehicle was administered at ZT 11.5, with the injection order counterbalanced. Liraglutide (0.3 mg/kg) or saline was administered at ZT 10. Behavior was monitored for 4 hours starting at ZT 12. In the light cycle experiment, Danuglipron (30 mg/kg) or vehicle was administered at ZT 2.5, and behavior was recorded for 4 hours starting at ZT 3. During the 4-hour testing window, mice had *ad libitum* access to either SD or HFD, depending on the test condition. On HFD test days, HFD was replaced with SD immediately after the recording period. Danuglipron was not administered on consecutive days. Sensors in the PhenoTyper cages recorded the following metrics: food hopper head entries, water bottle spout licks, and full running wheel rotations. Behavioral sessions were recorded with top-down infrared cameras (Noldus) at a resolution of 960 x 540 pixels at 25 frames per second, in grayscale. Videos were cropped to 2-hour segments using Adobe Premiere Pro and re-encoded with H.264 compression via FFmpeg to ensure smooth playback and frame-seeking.

Machine-learning assisted pipeline

Animal pose estimation was performed on home cage monitoring videos of singly housed, free roaming mice with Social LEAP Estimates Animal Poses (SLEAP, v1.3.3)[60,61]. The following 9 keypoints were tracked: nose, left ear, right ear, center 1-5, and tail base. We labeled 10,770 frames from 18 videos under conditions similar to the experimental ones, splitting them into 9,693 training and 1,077 validation frames (90% split). We used a U-Net based neural network with a max stride of 32, 16 filters, and a rotation angle of ± 180. All other hyperparameters were default using the single animal pipeline. The trained model's average distance (ground truth vs prediction) was: 1.59 pixels, mean object keypoint similarity (OKS): 0.85, mean average precision (mAP): 0.81, and mean average recall (mAR): 0.84. Inferences were made on the first two hours of videos (ZT 12-14), as this period was significant in the sensor data. Flow tracking and default hyperparameters were used for inference. Representative heatmaps of the mouse nose keypoint

716 were generated in Python by cropping to remove the walls of the cage and creating 62 by 27 pixel
717 bins.
718
719 Keypoint Motion Sequencing (Keypoint-MoSeq)[60,61] was then used to identify behavioral syllables
720 using a probabilistic model from the input keypoint coordinates of 80 hours of home cage videos.
721 Four latent dimensions accounted for 90% of the variance in aligned and centered keypoint
722 coordinates. A kappa of 10^5 was chosen to maintain the desired syllable time-scale. Using this
723 parameter, an autoregressive hidden Markov model (AR-HMM) was first fit to the data, followed
724 by the full model fit. Keypoint-MoSeq identified 91 behavioral syllables; 46 accounted for ≥ 0.5%
725 of instances, while those with frequencies < 0.5% but ≥ 0.01% were included, and < 0.01% were
726 excluded.
727
728 To provide biologically meaningful interpretations, the syllables were grouped into broader
729 behavioral categories (Fig. S6) by two trained raters. Some syllables represented a combination
730 of behaviors or closely related actions that could not be distinguished due to the camera angle
731 (e.g., "groom/sniff"). Poor-quality syllables (~1% of the dataset), likely from keypoint tracking
732 issues under the wheel, were excluded from analysis.

733 To incorporate location context, the pixel coordinates of the food hopper, shelter, and water bottle
734 spout were defined in videos using the Python OpenCV package (OpenCV, 2024). Regions of
735 interest (ROIs) were established around these coordinates. SLEAP coordinates identified when
736 the mouse entered a specific ROI, with the nose keypoint for the food hopper and water bottle
737 spout, and center 3 for the shelter. Behaviors were categorized based on location, such as
738 distinguishing "sniff by food" from "sniff" outside the food hopper ROI.

739 This categorization resulted in 23 unique behaviors, which were further grouped into five general
740 categories: “move/explore,” “rest,” “groom,” “food-motivated behaviors,” and “drink.” On average,
741 these behaviors accounted for 98.3% of the total time in the two-hour video recordings for each
742 video (mouse × condition). For each video, we calculated the total time spent performing each of
743 the 23 behaviors. Additionally, the proportion of time each mouse spent on the five general
744 behavior categories was calculated relative to their total behavioral time.

745 Proportional differences were assessed using a beta-distributed generalized linear mixed-effects
746 model with mouse as a random effect. For the inactive phase, the model included main effects of
747 drug and diet and their interaction. Behavioral collinearity was addressed with PCA, and the top
748 three principal components (PC 1–3) were analyzed via repeated measures MANOVA.

749 To reveal global differences in behavior by condition, linear discriminant analysis (LDA) with three
750 components was applied to the behavior duration dataset. LDA identified the linear combinations
751 of behavioral features that best separated conditions. Separate plots were generated for dark and
752 light cycle conditions, using the same LDA model fit across all tested conditions. Groups were
753 also visualized in PC space (PC 1 and PC 2) as used in the MANOVA analysis. LDA was
754 performed using the scikit-learn package [80,81]. All Python code for these analyses is available on
755 GitHub.

756 **Electrophysiology recordings**
757 *Brain slice preparation*
758 Preparation of acute brain slices for patch-clamp electrophysiology experiments was modified
759 from standard protocols previously described[82,83,84]. Mice were anesthetized with isoflurane and
760 decapitated. The brains were rapidly removed and kept in chilled artificial cerebrospinal fluid
761 (ACSF) (0°C) containing (in mM): 125 NaCl, 2.5 KCl, 1.25 NaH_2PO_4, 2 $CaCl_2$, 1 $MgCl_2$, 0.5 L-

762 ascorbic acid, 10 glucose, 25 $NaHCO_3$, and 2 Na-pyruvate (osmolarity 310 mOsm). Slices were
763 continuously oxygenated with 95% O2 and 5% CO2 throughout the preparation. Coronal brain
764 sections, 300 µm, were prepared using a Leica Microsystems VT1200 vibratome. Slices were
765 collected and placed in ACSF warmed to 37°C for 30 minutes and then kept at room temperature
766 for up to 5 hours.
767
768 *Recordings*
769 Brain slices were placed in a chamber superfused (~2 mL/min) with continuously oxygenated
770 ACSF solution warmed to 32 ± 1°C. hGLP1R-expressing Central amygdala neurons were
771 identified by video microscopy based on the expression of eYFP marker. Whole-cell
772 electrophysiology recordings were performed using a Multiclamp 700B amplifier with signals
773 digitized by a Digidata 1550B digitizer. Currents were amplified, lowpass-filtered at 2 kHz, and
774 sampled at 35 kHz. Borosilicate electrodes were fabricated using a Brown-Flaming puller (model
775 P1000, Sutter Instruments) to have pipette resistances between 2.5 and 4.5 mΩ. Current-clamp
776 recordings of membrane potentials were collected in ACSF solution identical to that used for
777 preparation of brain slices. The internal solution contained the following (in mM): 120 K-gluconate,
778 10 NaCl, 2 $MgCl_2$, 0.5 K_2EGTA, 10 HEPES, 4 Na_2ATP, and 0.3 NaGTP, pH 7.2 (osmolarity 290
779 mOsm). Resting membrane potential was recorded as previously described (1,2). After 5 mins of
780 baseline membrane potential recordings 10 µm of danuglipron was perfused for 5 mins followed
781 by washout.
782
783 *Statistics*
784 Electrophysiology recordings were analyzed using ClampFit 11.2. All statistical comparisons were
785 made using the appropriate test in GraphPad Prism 9.5.0. For membrane, AP properties, and
786 amplitude underwent descriptive statistics followed by normality and lognormality test using
787 gaussian distribution. Data were assessed for normality using the D'Agostino-Pearson omnibus
788 normality test, Anderson-Darling test, Shapiro-Wilk test, and Kolmogorov-Smirnov test with Dallal-
789 Wilkinson-Lillie for P-values. Data were tested for outliers using the ROUT method, and statistical
790 outliers were not included in data analysis. Followed by Tukey's test with no gaussian distribution
791 creating a nonparametric t-test using Wilcoxon matched-pairs signed rank test to compare
792 responses caused by the drug. Data are presented as individual data points and/or mean ± SEM.
793
794 **Fiber Photometry Recordings**
795 ***In vivo* calcium recording (GCaMP)**
796 Mice underwent 20-minute daily habituation sessions over two consecutive days to acclimate to
797 the fiber-optic cable (Doric Lenses, Ø400-µm core, 0.57 numerical aperture). On the test day,
798 mice were injected with either vehicle, saline, danuglipron (30 mg/kg) or liraglutide (0.3 mg/kg)
799 two hours prior to recording. The order of injections was randomized to avoid order effects.
800 Following the two-hour post-injection period, mice were connected to patch cables which were
801 interfaced with rotary joints to enable free movement. Recordings were conducted for one hour.
802 Fiber photometry data were recorded using fluorescent signals from both calcium-dependent (465
803 nm) and calcium-independent isosbestic (405 nm) excitation wavelengths (Doric). The isosbestic
804 (405 nm) signal served to control for artifacts. The light power of the fiber optic cable was
805 measured before each experiment and maintained at approximately 20-30 µW for both the
806 calcium-independent isosbestic (405 nm) and calcium-dependent (465 nm) signals.
807
808 ***In vivo* calcium analysis (GCaMP)**
809 The isosbestic signal (405 nm) was fitted to the calcium-dependent (465 nm) signal using a linear
810 least squares method implemented in a custom MATLAB script. Then ΔF/F was calculated as
811 (465 nm – fitted 405 nm) / fitted 405 nm. For significant calcium event detection analysis, we used
812 a combination of methodologies previously described [85]. Events were detected using a threshold

defined as the median plus two standard deviations of the entire recording, with events required to be 1.5 seconds or longer. The number of events detected per trial was then extracted and reported alongside heatmaps as %ΔF/F of entire recordings. Heatmaps were generated in Python using Min-Max normalization, scaled to a range of 0–1. For each mouse, the normalization range was determined based on the Vehicle condition: the average of the lowest 360 data points was set as the minimum, and the average of the highest 360 data points was set as the maximum. This normalization range, derived from the Vehicle condition, was then applied to the corresponding paired Danuglipron data for the same mouse. A moving average with a window and bin size of 10 smoothed the data, which was then plotted as a heatmap. Mice with missed virus injection or off-target fiber placement were excluded from analysis.

In vivo dopamine recording (dLight1.3b)

Mice were single-housed and habituated to the fiber optic cable and high-fat diet (HFD) for one hour over two consecutive days. On the test day, mice received an injection of either a drug (liraglutide [0.3 mg/kg], danuglipron [30 mg/kg], or orforglipron [1mg/kg]) or vehicle/saline, with the order of drug versus vehicle/saline injections randomized. Liraglutide and danuglipron were administered two hours before recording, while orforglipron was given four hours prior. Fiber photometry data were recorded as described above. Fluorescent signals were collected from both dopamine-dependent (465 nm) and dopamine-independent isosbestic (405 nm) excitation wavelengths. During the testing sessions, small pellets of HFD (~10 mg) were dropped into a cup at two-minute intervals after the mice retrieved the pellet. 5 to 6 trials were conducted per mouse. The recording session was video recorded to timestamp food retrieval time. Dopamine recordings were conducted during the light phase, between ZT3 and ZT6.

In vivo dopamine analysis (dLight1.3b)

The isosbestic signal (405 nm) was fitted to the dopamine-dependent (465 nm) signal using a linear least squares method implemented in a custom MATLAB script. Then ΔF/F was calculated as (465 nm – fitted 405 nm) / fitted 405 nm. To account for inter-animal differences in signal intensities, Z-scores were calculated for the ΔF/F signals. The baseline period for each food trial was defined as the 30-second interval prior to food retrieval. The mean and standard deviation of the baseline period were used to compute the Z-scores, with the formula: *Z* score = (F-Fμ(baseline))/std(baseline), where F is the 405 nm corrected 465 nm signal (ΔF/F), μ(baseline) is the mean, and std is the standard deviation of the baseline period. Video frames were analyzed to determine the exact timestamp when the mouse retrieved the pellet, which was defined as time 0 for each retrieval. The 30-second window centered around the food retrieval time was extracted. The area under the curve (AUC) and maximum fluorescence Z-scored within the food retrieval window was further extracted and analyzed for quantification of dopaminergic activity. 5 food trials were averaged per mouse. Mice with missed virus injections or off-target fiber placements were excluded from the analysis.

Statistical analyses

All data are presented as mean ±SEM unless otherwise noted. Statistical tests including paired or unpaired two-tailed t-tests, Kruskal-Wallis tests, Wilcoxon signed-rank tests, Pearson regression, one-way ANOVA, two-way/repeated-measures ANOVA (with Bonferroni correction or Tukey's HSD post hoc tests), MANOVA (with MATS resampling), linear mixed effect models with beta regression (with Tukey's post hoc test) were performed using RStudio (v4.3.0), Python (v3.11.5), JupyterLab (v3.6.3), MATLAB (R2023a), or GraphPad Prism (v10.4.0). Brief descriptions of all experiments in each figure panel, sample sizes, mean ±SEM, statistical test, test statistics, and *P*-values are presented in Supplementary Table 1. **P* <0.05; ***P* <0.01; ****P* <0.001.

Data availability

All data will be available on Dryad upon publication and select code will also be available on Github at https://github.com/UVACircMetNeuLab.

871 **References**

872 1. Wilding, J. P. H. *et al.* Once-Weekly Semaglutide in Adults with Overweight or Obesity. *N.*
873 *Engl. J. Med.* **384**, 989–1002 (2021).
874 2. Dharmalingam, M., Sriram, U. & Baruah, M. P. Liraglutide: A review of its therapeutic use as
875 a once daily GLP-1 analog for the management of type 2 diabetes mellitus. *Indian J.*
876 *Endocrinol. Metab.* **15**, 9–17 (2011).
877 3. Drucker, D. J. & Nauck, M. A. The incretin system: glucagon-like peptide-1 receptor agonists
878 and dipeptidyl peptidase-4 inhibitors in type 2 diabetes. *Lancet* **368**, 1696–1705 (2006).
879 4. Knudsen, L. B. & Lau, J. The discovery and development of liraglutide and semaglutide.
880 *Front Endocrinol (Lausanne)* **10**, 155 (2019).
881 5. Pi-Sunyer, X. *et al.* A randomized, controlled trial of 3.0 mg of liraglutide in weight
882 management. *N. Engl. J. Med.* **373**, 11–22 (2015).
883 6. Drucker, D. J. Mechanisms of Action and Therapeutic Application of Glucagon-like Peptide-
884 1. *Cell Metab.* **27**, 740–756 (2018).
885 7. Loomba, R. *et al.* Tirzepatide for Metabolic Dysfunction-Associated Steatohepatitis with
886 Liver Fibrosis. *N. Engl. J. Med.* **391**, 299–310 (2024).
887 8. Abushamat, L. A., Shah, P. A., Eckel, R. H., Harrison, S. A. & Barb, D. The Emerging Role
888 of Glucagon-Like Peptide-1 Receptor Agonists for the Treatment of Metabolic Dysfunction-
889 Associated Steatohepatitis. *Clin. Gastroenterol. Hepatol.* **22**, 1565–1574 (2024).
890 9. Bosch, C., Carriazo, S., Soler, M. J., Ortiz, A. & Fernandez-Fernandez, B. Tirzepatide and
891 prevention of chronic kidney disease. *Clin. Kidney J.* **16**, 797–808 (2023).
892 10. Perkovic, V. *et al.* Effects of Semaglutide on Chronic Kidney Disease in Patients with Type 2
893 Diabetes. *N. Engl. J. Med.* **391**, 109–121 (2024).
894 11. Nowell, J., Blunt, E. & Edison, P. Incretin and insulin signaling as novel therapeutic targets
895 for Alzheimer's and Parkinson's disease. *Mol. Psychiatry* **28**, 217–229 (2023).
896 12. Kopp, K. O., Glotfelty, E. J., Li, Y. & Greig, N. H. Glucagon-like peptide-1 (GLP-1) receptor

897 agonists and neuroinflammation: Implications for neurodegenerative disease treatment.
898 *Pharmacol. Res.* **186**, 106550 (2022).
899 13. Drucker, D. J. The benefits of GLP-1 drugs beyond obesity. *Science* **385**, 258–260 (2024).
900 14. Wang, W. *et al.* Associations of semaglutide with incidence and recurrence of alcohol use
901 disorder in real-world population. *Nat. Commun.* **15**, 4548 (2024).
902 15. Quddos, F. *et al.* Semaglutide and Tirzepatide reduce alcohol consumption in individuals
903 with obesity. *Sci. Rep.* **13**, 20998 (2023).
904 16. Wang, W. *et al.* Association of semaglutide with reduced incidence and relapse of cannabis
905 use disorder in real-world populations: a retrospective cohort study. *Mol. Psychiatry* **29**,
906 2587–2598 (2024).
907 17. Arillotta, D. *et al.* Exploring the Potential Impact of GLP-1 Receptor Agonists on Substance
908 Use, Compulsive Behavior, and Libido: Insights from Social Media Using a Mixed-Methods
909 Approach. *Brain Sci.* **14**, (2024).
910 18. Baggio, L. L. & Drucker, D. J. Glucagon-like peptide-1 receptors in the brain: controlling food
911 intake and body weight. *The Journal of Clinical Investigation* (2014).
912 19. Salinas, C. B. G. *et al.* Integrated brain atlas for unbiased mapping of nervous system
913 effects following liraglutide treatment. *Sci. Rep.* **8**, 10310 (2018).
914 20. Secher, A. *et al.* The arcuate nucleus mediates GLP-1 receptor agonist liraglutide-
915 dependent weight loss. *J. Clin. Invest.* **124**, 4473–4488 (2014).
916 21. Sisley, S. *et al.* Neuronal GLP1R mediates liraglutide's anorectic but not glucose-lowering
917 effect. *The Journal of Clinical Investigation* (2014).
918 22. Adams, J. M. *et al.* Liraglutide Modulates Appetite and Body Weight Through Glucagon-Like
919 Peptide 1 Receptor-Expressing Glutamatergic Neurons. *Diabetes* **67**, 1538–1548 (2018).
920 23. Huang, K.-P. *et al.* Dissociable hindbrain GLP1R circuits for satiety and aversion. *Nature*
921 **632**, 585–593 (2024).
922 24. Kim, K. S. *et al.* GLP-1 increases preingestive satiation via hypothalamic circuits in mice and

923 humans. *Science* **385**, 438–446 (2024).
924 25. Webster, A. N. *et al.* Molecular Connectomics Reveals a Glucagon-Like Peptide 1 Sensitive
925 Neural Circuit for Satiety. *BioRxiv* (2024) doi:10.1101/2023.10.31.564990.
926 26. FDA clarifies policies for compounders as national GLP-1 supply begins to stabilize | FDA.
927 https://www.fda.gov/drugs/drug-safety-and-availability/fda-clarifies-policies-compounders-
928 national-glp-1-supply-begins-stabilize.
929 27. Whitley, H. P., Trujillo, J. M. & Neumiller, J. J. Special Report: Potential Strategies for
930 Addressing GLP-1 and Dual GLP-1/GIP Receptor Agonist Shortages. *Clin. Diabetes* **41**,
931 467–473 (2023).
932 28. Chandrashekar, C. *et al.* Engineering of a Biologically Active Glycosylated Glucagon-Like
933 Peptide-1 Analogue. *J. Med. Chem.* **67**, 7276–7282 (2024).
934 29. Barredo-Vacchelli, G. R., Rodríguez, J. A., Eloy, J. A. & Camperi, S. A. A novel method for
935 liraglutide synthesis and purification. *Peptide Science* **116**, (2024).
936 30. He, J. & Chu, Y. Small-molecule GLP-1 secretagogs: challenges and recent advances. *Drug*
937 *Discov. Today* (2020) doi:10.1016/j.drudis.2020.08.003.
938 31. Dave Ricks, CEO of Eli Lilly | The All-In Interview - YouTube.
939 https://youtu.be/023exhA9irY?si=zvw1aQ6cVXtNlfy5&t=2181.
940 32. Wharton, S. *et al.* Daily Oral GLP-1 Receptor Agonist Orforglipron for Adults with Obesity. *N.*
941 *Engl. J. Med.* **389**, 877–888 (2023).
942 33. Dutta, D. *et al.* Orforglipron, a novel non-peptide oral daily glucagon-like peptide-1 receptor
943 agonist as an anti-obesity medicine: A systematic review and meta-analysis. *Obes. Sci.*
944 *Pract.* **10**, e743 (2024).
945 34. Eli Lilly and Company Q3 2024 Earnings Call. *Eli Lilly and Company Q3 2024 Earnings Call*
946 https://investor.lilly.com/static-files/cdedba2e-c4a7-4047-9e61-4ac3b1e2cd73 (2024).
947 35. Saxena, A. R. *et al.* Danuglipron (PF-06882961) in type 2 diabetes: a randomized, placebo-
948 controlled, multiple ascending-dose phase 1 trial. *Nat. Med.* **27**, 1079–1087 (2021).

949 36. Saxena, A. R. *et al.* Efficacy and Safety of Oral Small Molecule Glucagon-Like Peptide 1
950 Receptor Agonist Danuglipron for Glycemic Control Among Patients With Type 2 Diabetes:
951 A Randomized Clinical Trial. *JAMA Netw. Open* **6**, e2314493 (2023).
952 37. Griffith, D. A. *et al.* A Small-Molecule Oral Agonist of the Human Glucagon-like Peptide-1
953 Receptor. *J. Med. Chem.* **65**, 8208–8226 (2022).
954 38. Zhang, X. *et al.* Differential GLP-1R Binding and Activation by Peptide and Non-peptide
955 Agonists. *Mol. Cell* **80**, 485-500.e7 (2020).
956 39. Kawai, T. *et al.* Structural basis for GLP-1 receptor activation by LY3502970, an orally active
957 nonpeptide agonist. *Proc Natl Acad Sci USA* **117**, 29959–29967 (2020).
958 40. Search for: Other terms: orforglipron, Phase: 3 | Card Results | ClinicalTrials.gov.
959 https://clinicaltrials.gov/search?term=orforglipron&aggFilters=phase:3.
960 41. Arillotta, D. *et al.* GLP-1 Receptor Agonists and Related Mental Health Issues; Insights from
961 a Range of Social Media Platforms Using a Mixed-Methods Approach. *Brain Sci.* **13**, (2023).
962 42. Kornelius, E., Huang, J.-Y., Lo, S.-C., Huang, C.-N. & Yang, Y.-S. The risk of depression,
963 anxiety, and suicidal behavior in patients with obesity on glucagon like peptide-1 receptor
964 agonist therapy. *Sci. Rep.* **14**, 24433 (2024).
965 43. Chen, X., Zhao, P., Wang, W., Guo, L. & Pan, Q. The Antidepressant Effects of GLP-1
966 Receptor Agonists: A Systematic Review and Meta-Analysis. *Am. J. Geriatr. Psychiatry* **32**,
967 117–127 (2024).
968 44. Engel, J. A. & Jerlhag, E. Role of appetite-regulating peptides in the pathophysiology of
969 addiction: implications for pharmacotherapy. *CNS Drugs* **28**, 875–886 (2014).
970 45. Skibicka, K. P. The central GLP-1: implications for food and drug reward. *Front. Neurosci.* **7**,
971 181 (2013).
972 46. Falk, S. *et al.* GLP-1 and nicotine combination therapy engages hypothalamic and
973 mesolimbic pathways to reverse obesity. *Cell Rep.* **42**, 112466 (2023).
974 47. Jastreboff, A. M. *et al.* Tirzepatide once weekly for the treatment of obesity. *N. Engl. J. Med.*

975 **387**, 205–216 (2022).
976 48. Grippo, R. M. *et al.* Dopamine Signaling in the Suprachiasmatic Nucleus Enables Weight
977 Gain Associated with Hedonic Feeding. *Curr. Biol.* **30**, 196-208.e8 (2020).
978 49. Ahn, B. H., Kim, M. & Kim, S.-Y. Brain circuits for promoting homeostatic and non-
979 homeostatic appetites. *Exp. Mol. Med.* **54**, 349–357 (2022).
980 50. Liu, C. M. & Kanoski, S. E. Homeostatic and non-homeostatic controls of feeding behavior:
981 Distinct vs. common neural systems. *Physiol. Behav.* **193**, 223–231 (2018).
982 51. Gabery, S. *et al.* Semaglutide lowers body weight in rodents via distributed neural pathways.
983 *JCI Insight* **5**, (2020).
984 52. Alhadeff, A. L. *et al.* Endogenous Glucagon-like Peptide-1 Receptor Signaling in the
985 Nucleus Tractus Solitarius is Required for Food Intake Control. *Neuropsychopharmacology*
986 **42**, 1471–1479 (2017).
987 53. Zeng, N. *et al.* Anatomical and Functional Characterization of Central Amygdala Glucagon-
988 Like Peptide 1 Receptor Expressing Neurons. *Front. Behav. Neurosci.* **15**, 724030 (2021).
989 54. Liu, J. *et al.* Enhanced AMPA Receptor Trafficking Mediates the Anorexigenic Effect of
990 Endogenous Glucagon-like Peptide-1 in the Paraventricular Hypothalamus. *Neuron* **96**, 897-
991 909.e5 (2017).
992 55. Hansen, H. H. *et al.* Whole-brain activation signatures of weight-lowering drugs. *Mol. Metab.*
993 **47**, 101171 (2021).
994 56. Petersen, J. *et al.* GLP-1-directed NMDA receptor antagonism for obesity treatment. *Nature*
995 **629**, 1133–1141 (2024).
996 57. Zhang, C. *et al.* Area Postrema Cell Types that Mediate Nausea-Associated Behaviors.
997 *Neuron* **109**, 461-472.e5 (2021).
998 58. Pfizer Nixes Twice-Daily Oral GLP-1 Candidate After High Rates of Side Effects - BioSpace.
999 https://www.biospace.com/pfizer-nixes-twice-daily-oral-glp-1-candidate-after-high-rates-of-
1000 side-effects.

1001 59. Lean, M. E. J. *et al.* Tolerability of nausea and vomiting and associations with weight loss in
1002 a randomized trial of liraglutide in obese, non-diabetic adults. *Int J Obes (Lond)* **38**, 689–697
1003 (2014).
1004 60. Pereira, T. D. *et al.* SLEAP: A deep learning system for multi-animal pose tracking. *Nat.*
1005 *Methods* **19**, 486–495 (2022).
1006 61. Weinreb, C. *et al.* Keypoint-MoSeq: parsing behavior by linking point tracking to pose
1007 dynamics. *Nat. Methods* **21**, 1329–1339 (2024).
1008 62. Rodgers, R. J., Holch, P. & Tallett, A. J. Behavioural satiety sequence (BSS): separating
1009 wheat from chaff in the behavioural pharmacology of appetite. *Pharmacol. Biochem. Behav.*
1010 **97**, 3–14 (2010).
1011 63. Lee, S. J. *et al.* Loss of dorsomedial hypothalamic GLP-1 signaling reduces BAT
1012 thermogenesis and increases adiposity. *Mol. Metab.* **11**, 33–46 (2018).
1013 64. Harikumar, K. G. *et al.* Glucagon-like peptide-1 receptor dimerization differentially regulates
1014 agonist signaling but does not affect small molecule allostery. *Proc Natl Acad Sci USA* **109**,
1015 18607–18612 (2012).
1016 65. Choe, H. J. & Cho, Y. M. Peptidyl and Non-Peptidyl Oral Glucagon-Like Peptide-1 Receptor
1017 Agonists. *Endocrinol Metab (Seoul)* **36**, 22–29 (2021).
1018 66. Zheng, Z. *et al.* Glucagon-like peptide-1 receptor: mechanisms and advances in therapy.
1019 *Signal Transduct. Target. Ther.* **9**, 234 (2024).
1020 67. Zhang, H. *et al.* Binding sites and design strategies for small molecule GLP-1R agonists.
1021 *Eur. J. Med. Chem.* **275**, 116632 (2024).
1022 68. Wang, H. *et al.* Parallel gut-to-brain pathways orchestrate feeding behaviors. *Nat. Neurosci.*
1023 (2024) doi:10.1038/s41593-024-01828-8.
1024 69. Alhadeff, A. L., Rupprecht, L. E. & Hayes, M. R. GLP-1 neurons in the nucleus of the solitary
1025 tract project directly to the ventral tegmental area and nucleus accumbens to control for food
1026 intake. *Endocrinology* **153**, 647–658 (2012).

1027 70. Alhadeff, A. L. & Grill, H. J. Hindbrain nucleus tractus solitarius glucagon-like peptide-1
1028 receptor signaling reduces appetitive and motivational aspects of feeding. *Am. J. Physiol.*
1029 *Regul. Integr. Comp. Physiol.* **307**, R465-70 (2014).
1030 71. Merkel, R. *et al.* An endogenous GLP-1 circuit engages VTA GABA neurons to regulate
1031 mesolimbic dopamine neurons and attenuate cocaine seeking. *BioRxiv* (2024)
1032 doi:10.1101/2024.06.20.599574.
1033 72. Webster, A. N. *et al.* Molecular connectomics reveals a glucagon-like peptide 1-sensitive
1034 neural circuit for satiety. *Nat. Metab.* (2024) doi:10.1038/s42255-024-01168-8.
1035 73. Sisley, S. *et al.* Neuronal GLP1R mediates liraglutide's anorectic but not glucose-lowering
1036 effect. *J. Clin. Invest.* **124**, 2456–2463 (2014).
1037 74. Fortin, S. M. & Roitman, M. F. Central GLP-1 receptor activation modulates cocaine-evoked
1038 phasic dopamine signaling in the nucleus accumbens core. *Physiol. Behav.* **176**, 17–25
1039 (2017).
1040 75. Egecioglu, E., Engel, J. A. & Jerlhag, E. The glucagon-like peptide 1 analogue Exendin-4
1041 attenuates the nicotine-induced locomotor stimulation, accumbal dopamine release,
1042 conditioned place preference as well as the expression of locomotor sensitization in mice.
1043 *PLoS ONE* **8**, e77284 (2013).
1044 76. Kenny, P. J. Reward mechanisms in obesity: new insights and future directions. *Neuron* **69**,
1045 664–679 (2011).
1046 77. Klausen, M. K., Thomsen, M., Wortwein, G. & Fink-Jensen, A. The role of glucagon-like
1047 peptide 1 (GLP-1) in addictive disorders. *Br. J. Pharmacol.* **179**, 625–641 (2022).
1048 78. Vallöf, D. *et al.* The glucagon-like peptide 1 receptor agonist liraglutide attenuates the
1049 reinforcing properties of alcohol in rodents. *Addict. Biol.* **21**, 422–437 (2016).
1050 79. Botta, P. *et al.* An Amygdala Circuit Mediates Experience-Dependent Momentary Arrests
1051 during Exploration. *Cell* **183**, 605-619.e22 (2020).
1052 80. Alex, F., ALEX, G., Bertr, RE. GRAMFORTINRIA. F., BERTR, T. & THIRION. Scikit-learn:

1053 Machine Learning in Python.
1054 81. Wiltschko, A. B. *et al.* Revealing the structure of pharmacobehavioral space through motion
1055 sequencing. *Nat. Neurosci.* **23**, 1433–1443 (2020).
1056 82. Ottolini, M., Barker, B. S., Gaykema, R. P., Meisler, M. H. & Patel, M. K. Aberrant sodium
1057 channel currents and hyperexcitability of medial entorhinal cortex neurons in a mouse model
1058 of SCN8A encephalopathy. *J. Neurosci.* **37**, 7643–7655 (2017).
1059 83. Wengert, E. R. *et al.* Somatostatin-Positive Interneurons Contribute to Seizures in SCN8A
1060 Epileptic Encephalopathy. *J. Neurosci.* **41**, 9257–9273 (2021).
1061 84. Bunton-Stasyshyn, R. K. A. *et al.* Prominent role of forebrain excitatory neurons in SCN8A
1062 encephalopathy. *Brain* **142**, 362–375 (2019).
1063 85. Jones, J. R., Simon, T., Lones, L. & Herzog, E. D. SCN VIP Neurons Are Essential for
1064 Normal Light-Mediated Resetting of the Circadian System. *J. Neurosci.* **38**, 7986–7995
1065 (2018).
1066

Acknowledgements

We thank the members of the Güler, Deppmann, Campbell, and Provencio laboratories (University of Virginia) for comments and suggestions on the preparation of the manuscript. We are thankful for technical help from Stefani A. Mancuso and technical advice from Amrita Pathak, along with Anthony Spano (University of Virginia) who developed the three viral constructs. We thank Talmo Pereira (Salk Institute for Biological Studies) and Caleb Weinreb (Harvard Medical School) for their technical advice. We thank the Genetically Engineered Murine Model (GEMM) Core (University of Virginia) for aiding in the CRISPR-Cas9 development of our mouse model.

Funding: We used AI-assisted technologies (OpenAI, Anthropic) as an aid for drafting and grammar proofing the manuscript. This work was supported by NIH R35GM140854 (ADG), NIH R01NS111220 (CDD), NIH R01HL153916 and American Diabetes Association Pathway to Stop Diabetes Award 1-18-INI-14 (JNC), NIH R01 NS122834 (MKP), NIH R01 NS120702 (MKP), University of Virginia BRAIN Institute Seed Funding 2023 & 2024 (ADG, CDD) and 2024 & 2025 (ADG, JNC), University of Virginia BRAIN Institute Presidential Fellowship in Collaborative Neuroscience (ENG), University of Virginia National Science Foundation, EXPAND Traineeship (ENG), and the GEMM core partially supported by the funding of NIH-NCI CCSG P30 CA044579.

Author contributions

Conceptualization: ENG, TBG, IRS, ABK, JNC, CDD, ADG
Data curation: ENG, TBG, IRS, TCJD, SO, YZ
Formal analysis: ENG, TBG, IRS, TCJD, ADG
Funding acquisition: ENG, MKP, JNC, CDD, ADG
Investigation: ENG, TBG, IRS, YZ, YS, NJC, ANW, OYC, SO, AA, KM, KIW, AK, GG
Methodology: ENG, TBG, IRS, ABK, AKB
Project administration: ADG
Resources: MKP, JNC, CDD, ADG
Supervision: ENG, TBG, IRS, MKP, JNC, CDD, ADG
Validation: ENG, TBG, IRS, AKB, CDD, ADG
Visualization: ENG, TBG, IRS
Writing – original draft: ENG, TBG, IRS, CDD, ADG
Writing – review & editing: ENG, TBG, IRS, JNC, CDD, ADG

Competing interests: The authors declare that they have no competing interest.

Extended Data

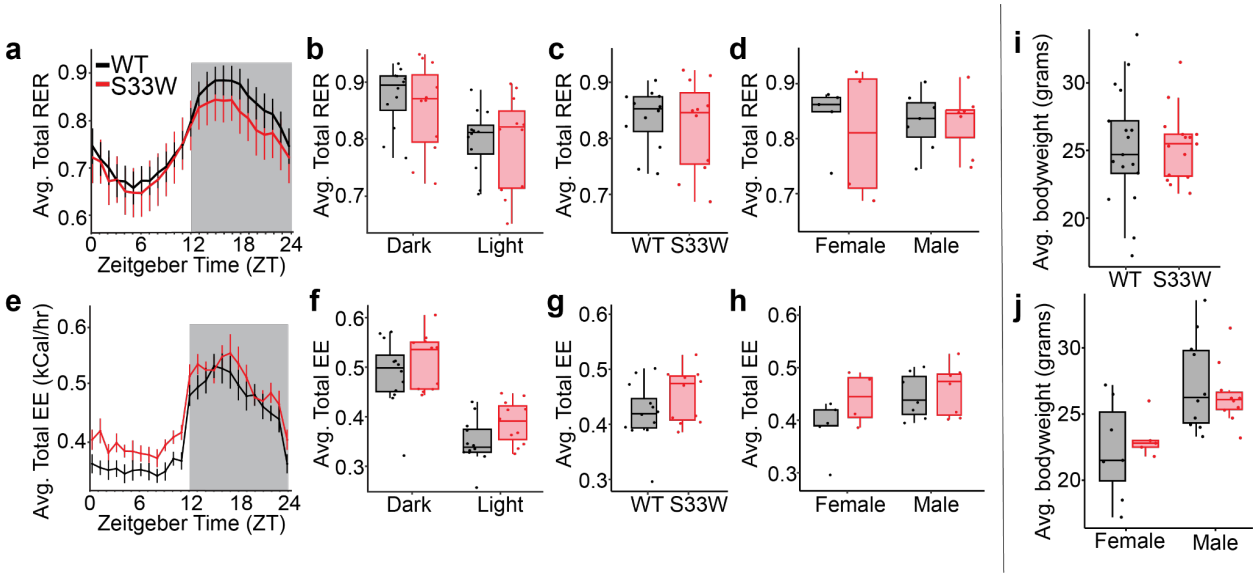

Extended Data Fig. 1. Metabolic profiling of WT and Glp1r^{S33W} mice. a,e, Diurnal rhythms averaged over 3 days of (**a**) respiratory exchange ratio (RER) and (**e**) energy expenditure (EE) in WT and Glp1r^{S33W} mice. **b-g**, Average dark/light phase and total 24 hour (**b,c**) RER and (**f,g**) EE between WT and Glp1r^{S33W} mice (n = 11-12 per genotype, two-way ANOVA with Bonferroni correction or Welch's t-test). **d,h**, Total 24 hour (**d**) RER and (**h**) EE averaged by sex (n = 4-5 females, n = 7 males per genotype, two-way ANOVA with Bonferroni correction). **i**, Average baseline body weight of WT and Glp1r^{S33W} mice 10 to 20 weeks old (n = 18-19 per genotype, Welch's t-test). **j**, Average baseline body weight of WT and Glp1r^{S33W} male and female mice (n = 8-9 females, n = 10 males per group, two-way ANOVA with Bonferroni correction). Data are represented as medians ± Q1-Q3. *P<0.05; **P<0.01; ***P<0.001.

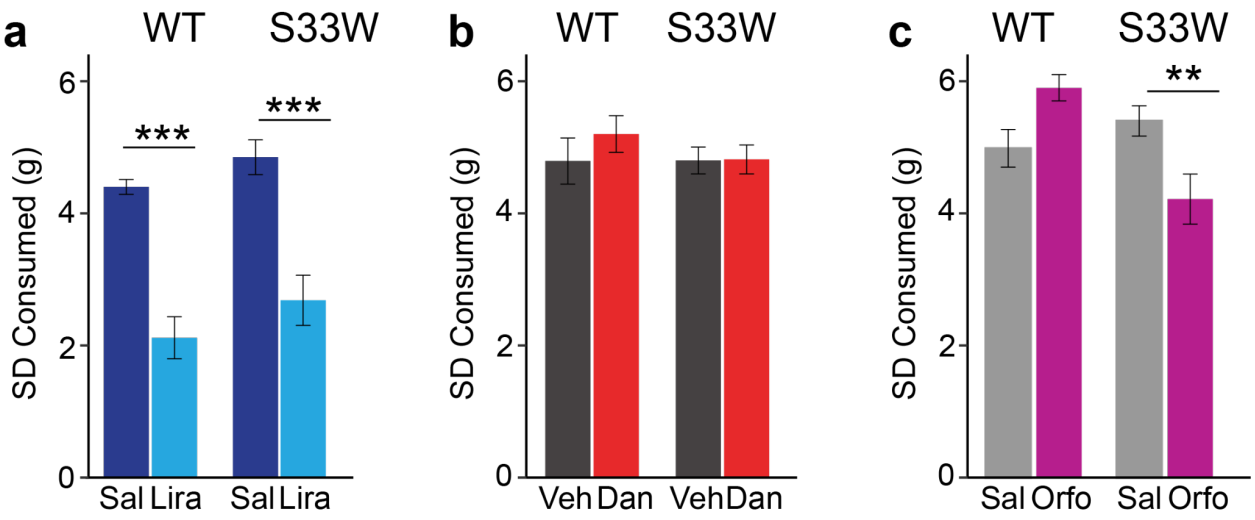

Extended Data Fig. 2. 24-hour effects of GLP1RAs on standard diet consumption. a-c, Standard diet (SD) consumption 24 hours after (**a**) liraglutide, (**b**) danuglipron, and (**c**) orforglipron injection in WT and Glp1r^{S33W} mice. (n = 6 per injection, two-way ANOVA with Bonferroni correction, $^{**}P<0.01$; $^{***}P<0.001$). Data are represented as means ± SEM.

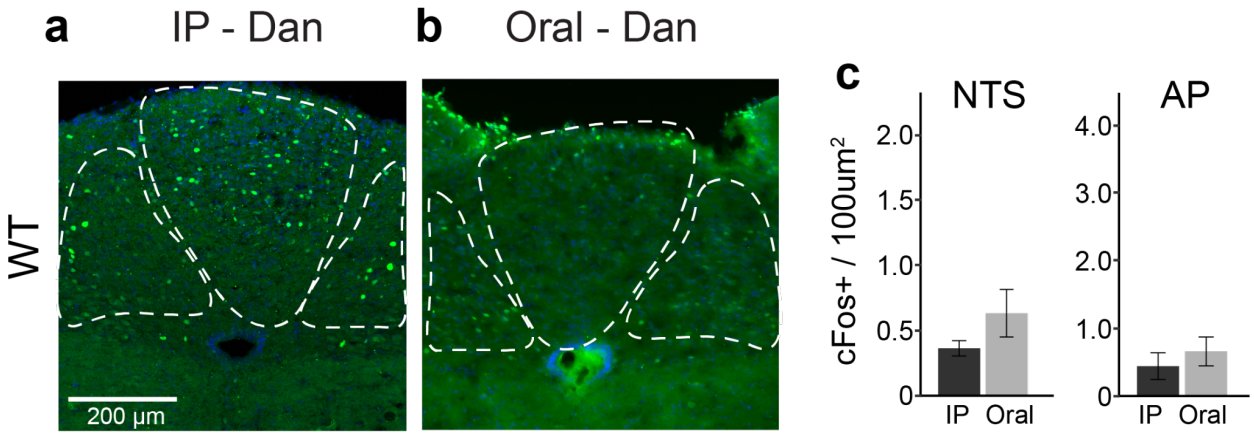

Extended Data Fig. 3. cFos activation in NTS and AP of WT mice administered oral or IP danuglipron. a,b, Neuronal cFos activation in the NTS and AP 2-hours after danuglipron was administered to WT mice via (**a**) IP injection or (**b**) oral gavage. **c**, Quantification of cFos expression in the NTS (left) or AP (right) following danuglipron IP or oral delivery in WT mice (*n* = 3-4 per delivery route, Welch's t-test). Data are represented as means ± SEM. **P*<0.05; ***P*<0.01; ****P*<0.001.

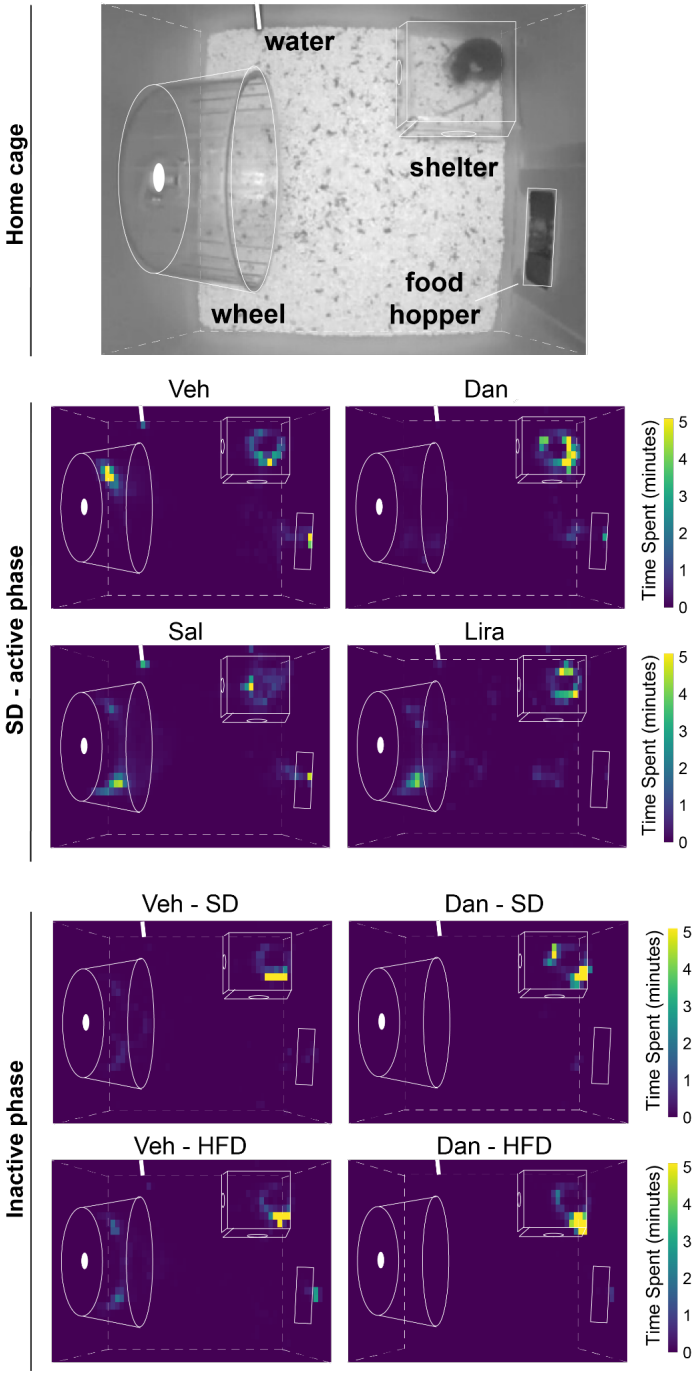

Extended Data Fig. 4. Home cage monitoring heatmaps of Glp1r^{S33W} mice. Representative image of home cage set-up (dimensions: 30 x 30 x 43.5 cm) with calibrated positions of wheel, IR translucent shelter (10.5 x 10.5 x 6 cm), food hopper (5.5 cm from floor), and water bottle spout (5 cm from floor) identified in white outline (top). Coordinate-based heatmaps of nose keypoint trajectories recorded at 25 fps over 2-hour sessions for each treatment group during active (ZT 12-14) or inactive (ZT 3-5) phase. Color scale represents dwelling time in seconds.

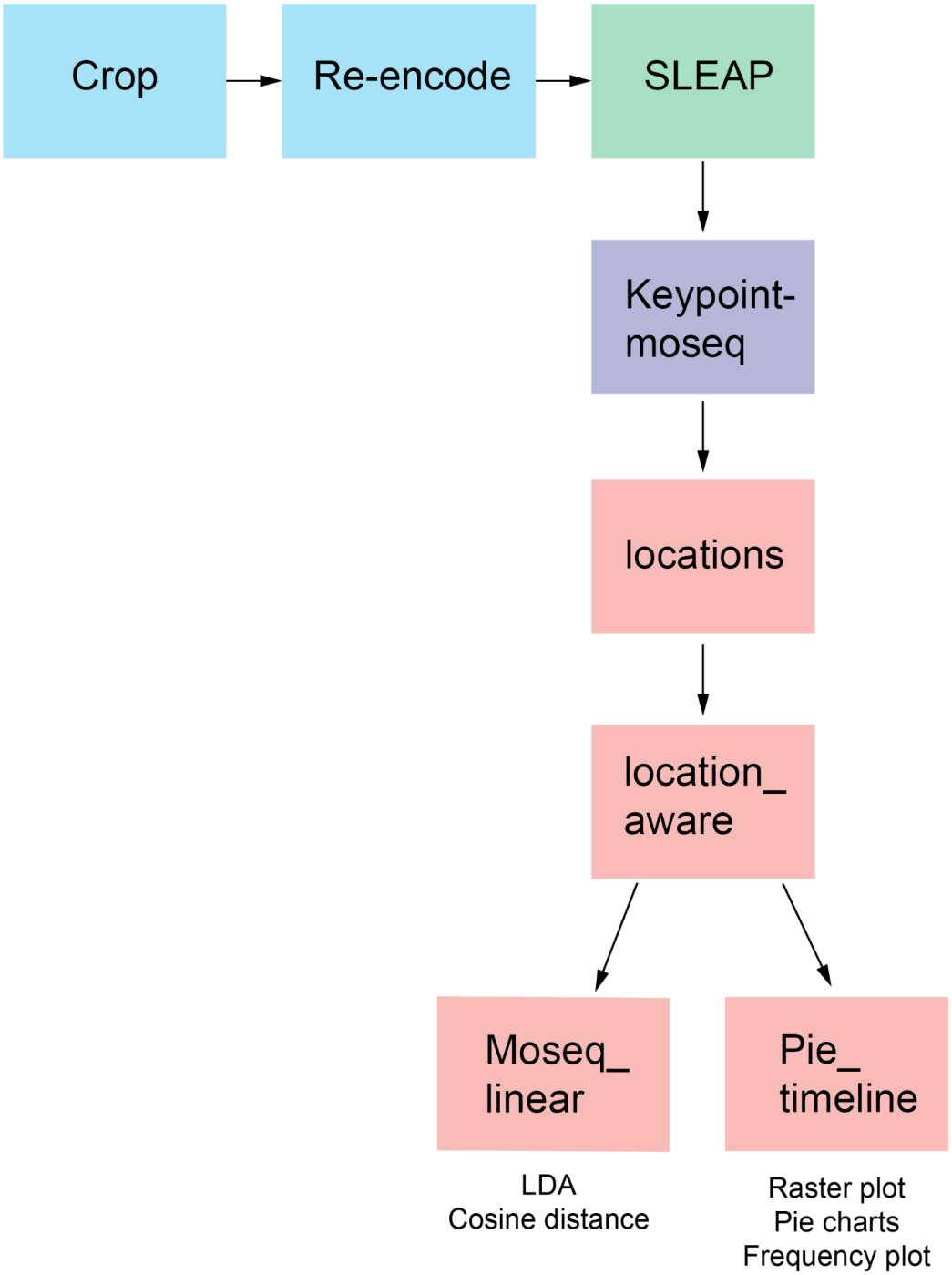

Extended Data Fig. 5. Machine-learning assisted pipeline for home cage behavioral analysis. Blue squares represent video pre-processing steps. Social LEAP Estimates Animal Poses (SLEAP) was used to extract nine keypoint coordinates for each mouse in the videos (Fig. 3, A to B; fig. S4). Keypoint Motion Sequencing (Keypoint-MoSeq) identified behavioral syllables from these coordinates (fig. S6). Red squares represent Python scripts used for the analysis of Keypoint-MoSeq syllable results: locations (identify regions of interest), location_aware (**Fig. 3c-n**), lda_cosine (**Fig. 3l,n**), and pie_timeline (**Fig. 3b,e,f,m**).

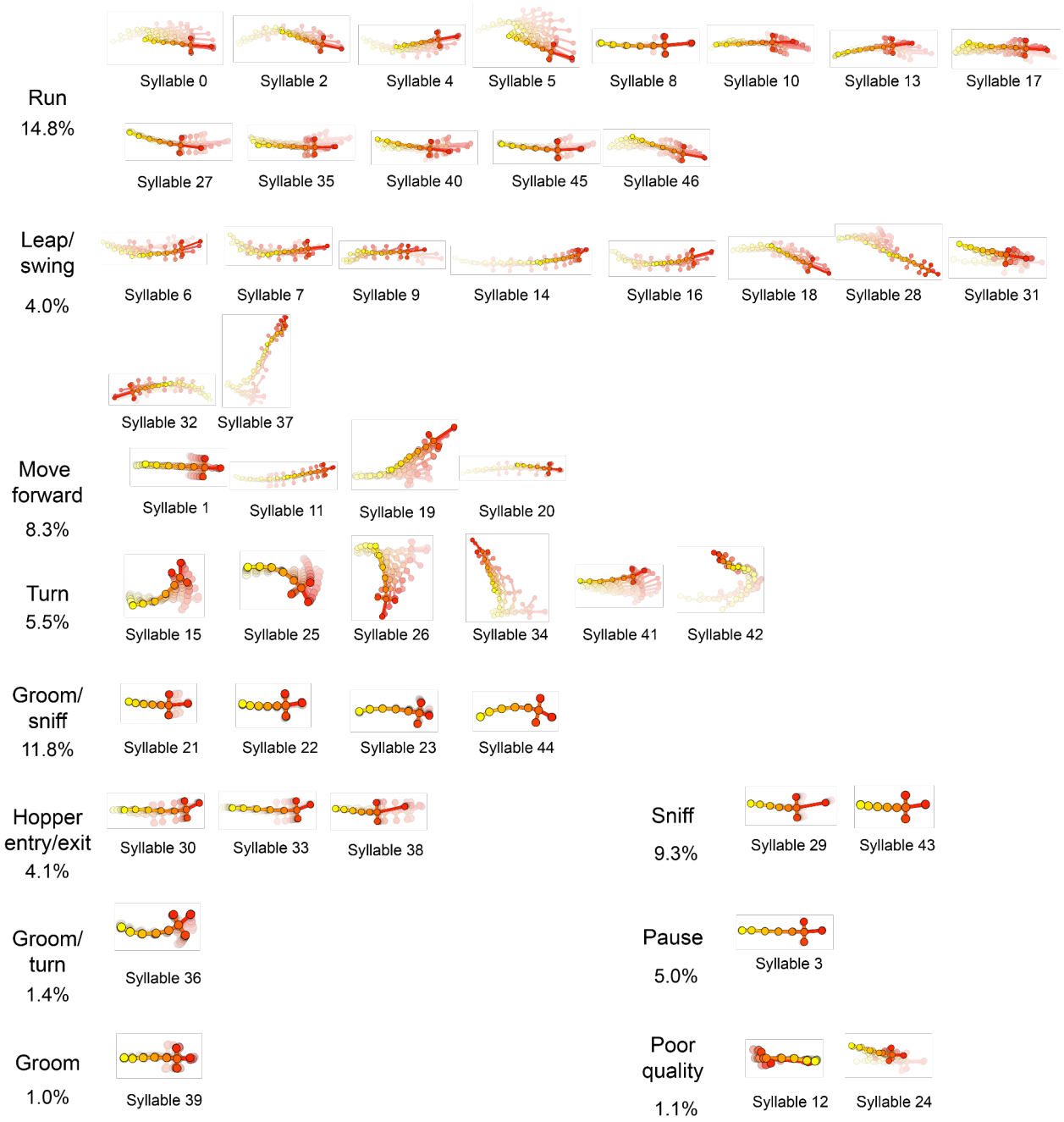

Extended Data Fig. 6. Trajectory plots of main behavioral syllables identified by Keypoint-MoSeq. Syllables identified from keypoint coordinates by Keypoint-MoSeq were sorted into 11 categories by trained raters using grid movies generated for each syllable. The proportion of each syllable category is presented as a percentage. Rare syllables (minimum frequency < 0.5% but ≥ 0.01%) are not visually depicted but were included in the analysis.

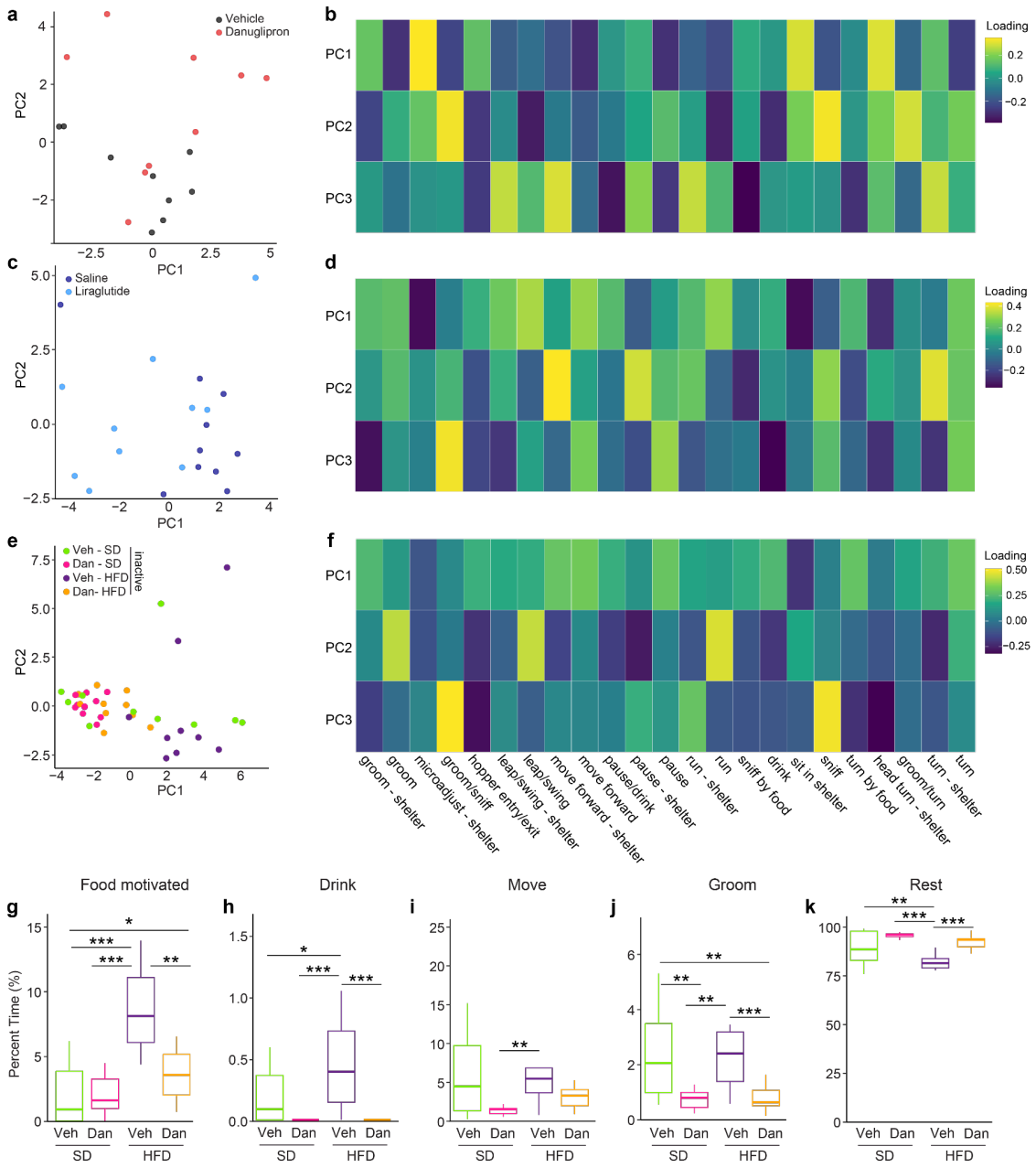

Extended Data Fig. 7. Principal component analysis and inactive phase behaviors. a–f, Principal Component Analysis (PCA) of 23 behavioral durations recorded during 2-hour home cage video sessions. PCA score plots for: (**a**) Vehicle and danuglipron-treated mice, (**c**) saline and liraglutide-treated mice, and (**e**) inactive-phase SD- and HFD-fed mice treated with vehicle or danuglipron. Corresponding PCA loading plots illustrating: (**b**) vehicle and danuglipron, (**d**) saline and liraglutide, and (**f**) inactive-phase SD- and HFD-fed mice treated with vehicle or danuglipron. **g–k**, Proportion of time allocated to five behavioral categories during the inactive phase for SD- and HFD-fed mice on vehicle or danuglipron: (**g**) food-motivated behaviors, (**h**) drinking, (**i**) movement/exploration, (**j**) grooming, and (**k**) resting behaviors (n = 10 per injection, (n = 10, generalized linear mixed-effects model (beta distribution) with main effects of drug and diet, as well as their interaction, followed by Tukey's post-hoc test, *P<0.05; **P<0.01; ***P<0.001). Data are represented as medians ± Q1-Q3. *P<0.05; **P<0.01; ***P<0.001.

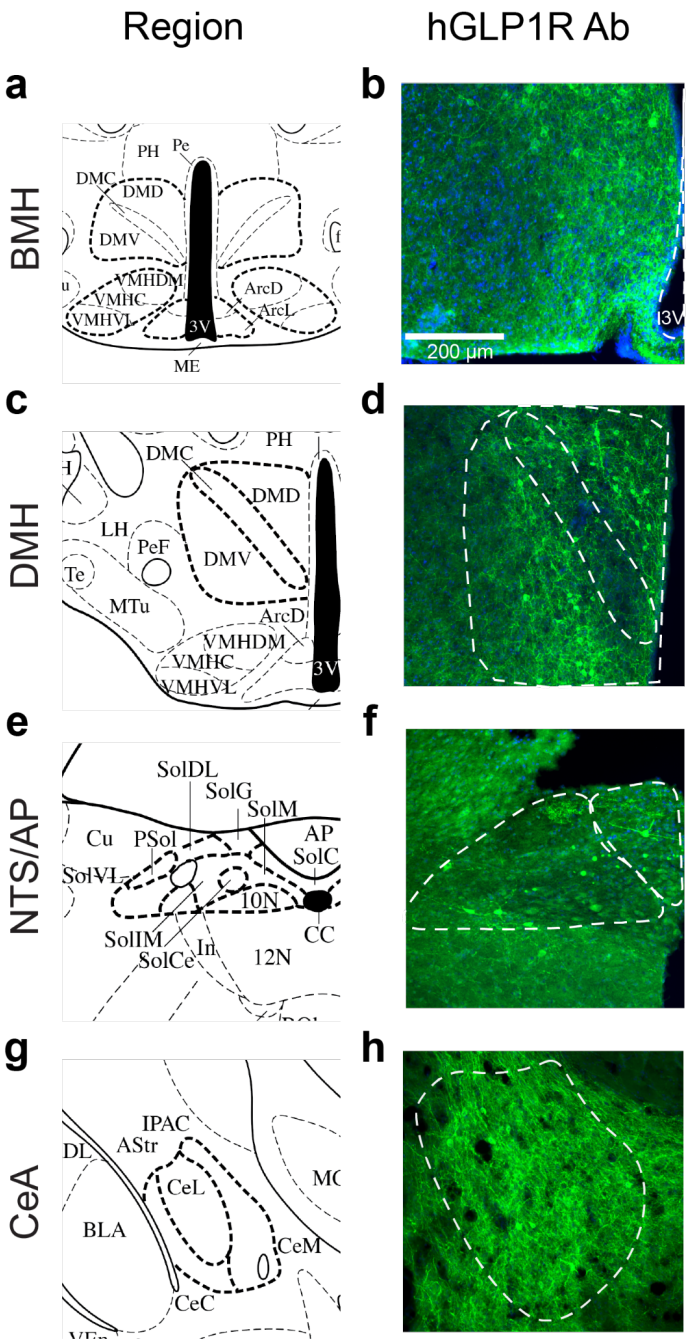

Extended Data Fig. 8. Validation of AAV-hSyn-DIO-hGLP1R virus. a-h, Fluorescent microscopy images of the brain regions stereotaxically injected with AAV-DIO-hGLP1R. Images from Allen Brain Atlas, with regions of interest in bold and hGLP1R antibody staining (green) in the (**a,b**) basomedial hypothalamus (BMH), (**c,d**) DMH, (**e,f**) NTS/AP, or (**g,h**) CeA. Scale bars = 200 µm.

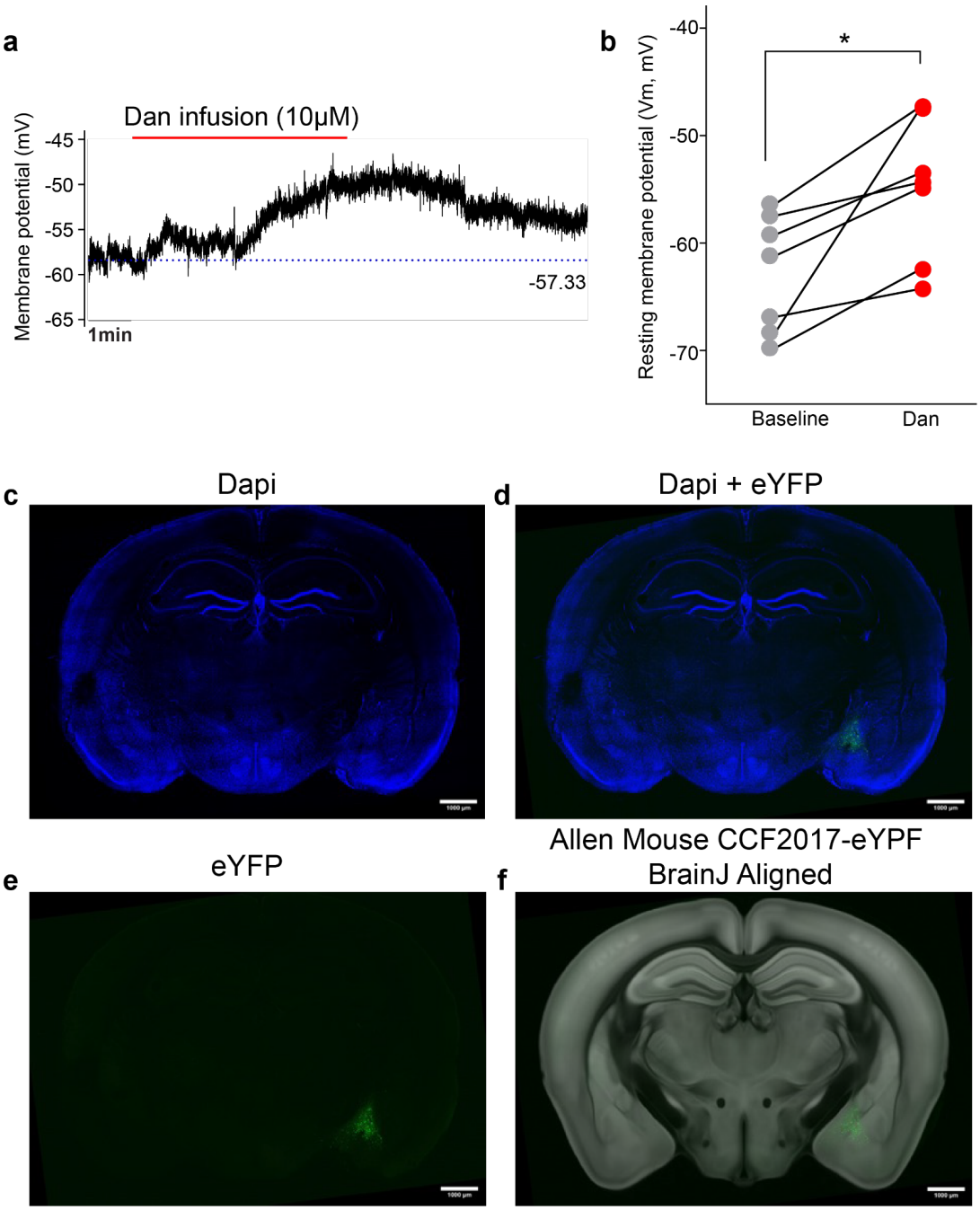

Extended Data Fig. 9. Danuglipron depolarizes the resting membrane potential in hGLP1R-expressing CeA neurons. a, Representative trace showing the effect of 5 minutes of danuglipron perfusion (10 μM) on the resting membrane potential of CeA neurons. **b,** Average depolarization induced by danuglipron compared to baseline recording. Baseline: −62.72 ± 2.08 mV; danuglipron: −54.87 ± 2.49 mV; average change: 7.8 mV (n = 7 cells, Wilcoxon signed-rank test, *P<0.05). **c–f,** Localization of eYFP-labeled hGLP1R-expressing neurons in the central amygdala (CeA). BrainJ software [79] analysis indicates prominent eYFP labeling in the capsular part of the CeA, with additional labeling in the lateral part. Scale bars = 1000 μm.

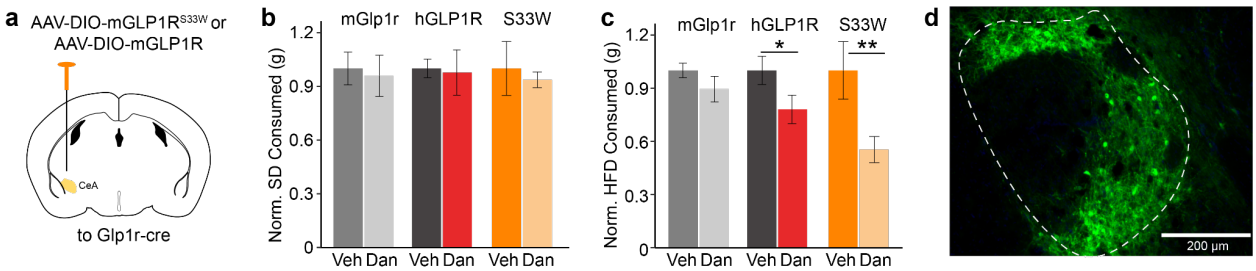

Extended Data Fig. 10. AAV-DIO-mGLP1R^{S33W}-HA targeted to the CeA of Glp1r-Cre mice recapitulates effects of AAV-DIO-hGLP1R. a, Schematic of Glp1r-Cre mice injected with a Cre-dependent AAV carrying full length mouse Glp1r (mGlp1r) or AAV carrying full length mouse GLP1R with the S33W mutation at position 33 (mGLP1R^{S33W}) in the CeA. **b,c**, Normalized 4-hour (**b**) SD and (**c**) HFD consumption post-injection of vehicle or danuglipron in mGlp1r, full length human GLP1R (hGLP1R) or mGlp1r-S33W (S33W) expressing mice (n = 4-9 per group, two-way ANOVA with Bonferroni correction, *P<0.05; **P<0.01). **d**, Representative image of AAV-DIO-mGLP1R^{S33W}-HA expression in the CeA (green). Scale bars = 200 µm. Data are represented as means ± SEM. *P<0.05; **P<0.01; ***P<0.001.

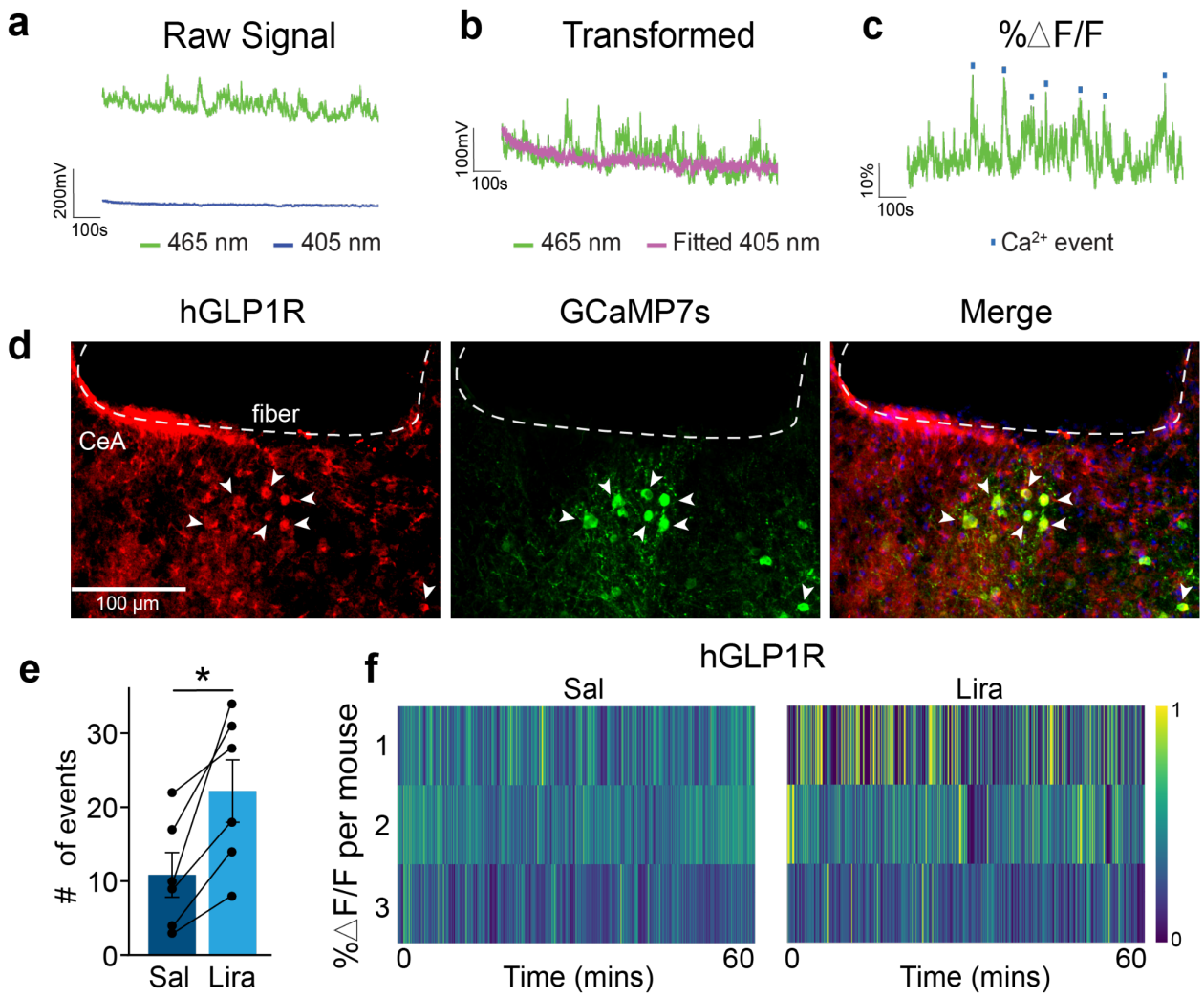

Extended Data Fig. 11. Fiber photometry recordings and validation of CeA^{GLP1R} neurons. a, Representative traces of fiber photometry recordings showing calcium-dependent fluorescence (465nm) and calcium-independent, isosbestic fluorescence (405nm) signals. **b**, Fitted 405nm signal (pink) transformed for ΔF/F calculation. **c,** Representative trace of %ΔF/F used for analysis. Blue dots indicate detected calcium events, identified using a threshold set at 2 standard deviations plus the median of the entire 1-hour recording session, with an event required to be longer than 1.5 seconds. **d**, Representative images of AAV-DIO-GCaMP7s + hGLP1R targeted to the CeA. Validation with hGLP1R antibody (red; left), GCaMP7s (green; middle), and verification of colocalization (right). Scale bars = 100 µm. **e**, Number of significant calcium events averaged per mouse during 1-hour recording session following saline or liraglutide in CeA-hGLP1R expressing mice (n = 6 per injection, paired t-test, *P<0.05). **f**, Representative heatmaps of %ΔF/F neuronal calcium signal per mouse during 1-hour of fiber photometry recording after saline (left) or liraglutide (right) injection in CeA-hGLP1R expressing mice. Data are represented as means ± SEM. *P<0.05; **P<0.01; ***P<0.001.

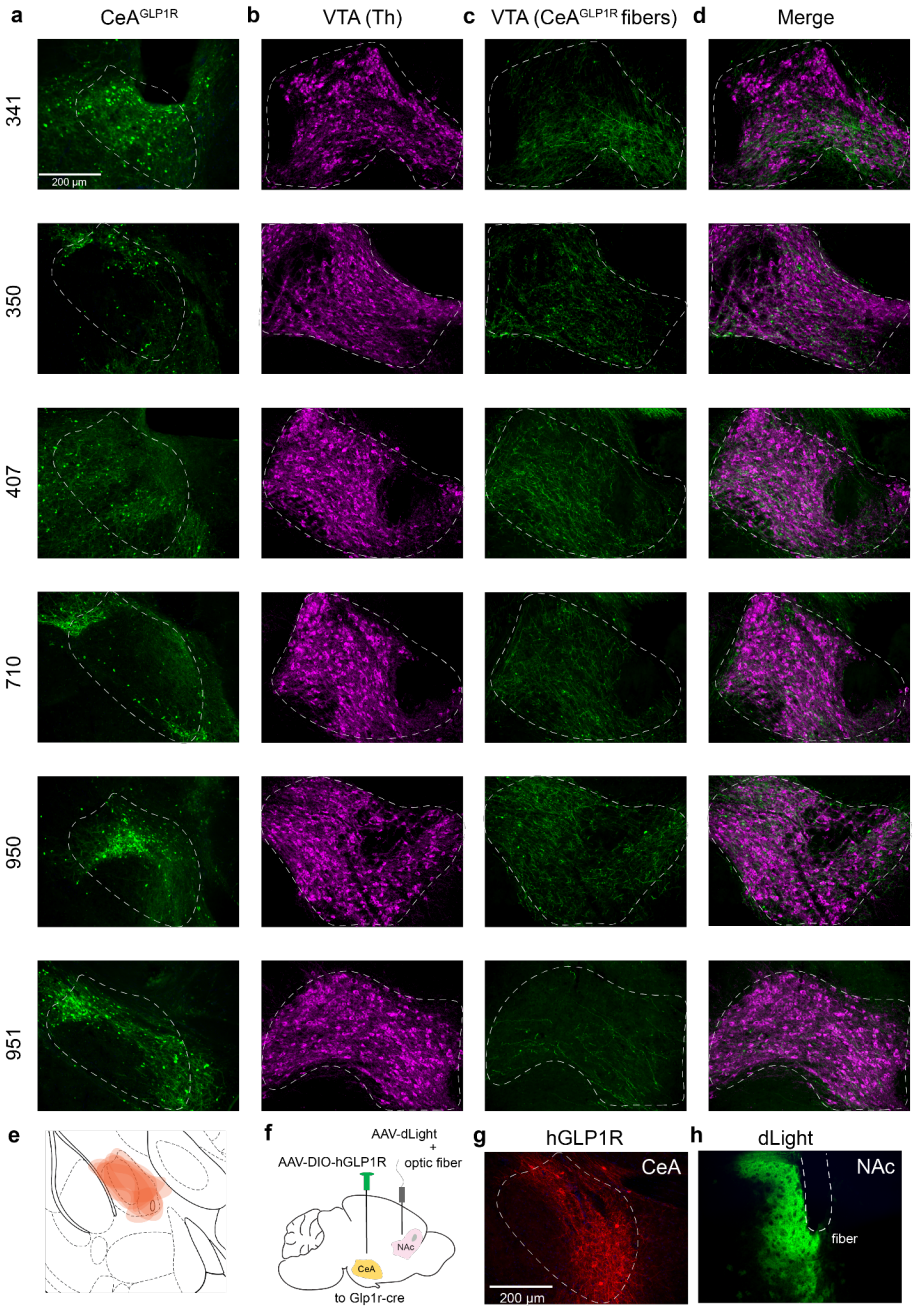

Extended Data Fig. 12. CeA^{GLP1R} neurons innervate the VTA and validation of AAVs targeting CeA and NAc. a, Representative images of AAV-DIO-ChR2-eYFP expression targeted to the CeA of Glp1r-Cre mice (green; *n* = 6). **b**, Tyrosine hydroxylase (Th) expression in the VTA (magenta). **c**, Axon fiber projections from CeA^{GLP1R} neurons into the VTA, and **d**, colocalization of Th with CeA^{GLP1R} fibers in the VTA. **e**, Traces of superimposed AAV-DIO-ChR2-eYFP injection targeting per mouse, collapsed on the Allen Brain Atlas figure. **f**, Schematic showing AAV-dLight1.3b injection into the NAc and AAV-DIO-hGLP1R injection into the CeA of Glp1r-Cre mice, with fiber optic implants in the NAc. **g**, Validation of AAV-DIO-hGLP1R targeting the CeA using hGLP1R antibody staining (red). **h**, Representative AAV-dLight expression in the NAc and fiber optic implant placement (green). Scale bars = 200 µm.

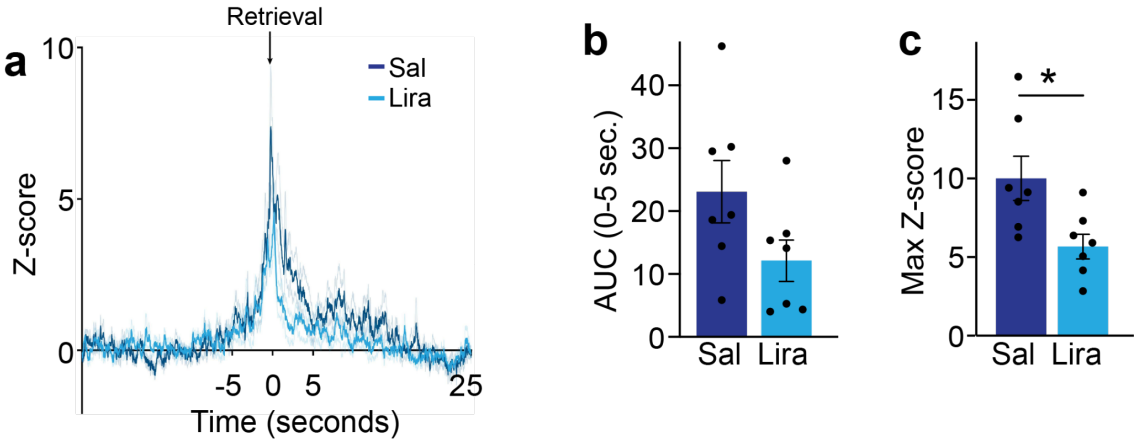

Extended Data Fig. 13. Liraglutide reduces NAc dopamine release in response to HFD. a, Averaged Z-score traces showing dopamine release in the NAc in response to HFD following administration of saline or liraglutide in Glp1r^{S33W} mice. Traces are aligned to food retrieval time (t = 0) and averaged across five food trials per mouse. **b,c**, Quantified (**b**) area under the curve (AUC) for Z-scores and (**c**) maximum fluorescence Z-scores within the food retrieval window (n = 7, paired t-test, *P<0.05). Data are represented as means ± SEM. *P<0.05; **P<0.01; ***P<0.001.